

Synthesis and functionalization of magnetic iron oxide nanocrystals

MASTERS THESIS, NANOBIO TECHNOLOGY

JAKOB JAKOBSSON

JUNE 10, 2019



AALBORG UNIVERSITY
STUDENT REPORT

**Final thesis for masters studies of
Nanobiotechnology at the School of
Engineering and Science**

The Faculty of Natural Sciences

Physics and Nanotechnology

Skjernvej 4a

9220 Aalborg Ø

Title:

Synthesis and functionalization of magnetic iron oxide nanocrystals

Project period:

September 2018 - June 2019

Participants:

Jakob Jakobsson

Supervisors:

Leonid Gurevich

Total pages: 60

Appendices: 1

Finalized 10-06-2019

Abstract:

In this project magnetic iron oxide nanoparticles were synthesized and modified for greater stability and imaging purposes. The particles were synthesized using two methods, co precipitation and thermal decomposition. Dynamic light scattering showed the particles to be between 15-40nm depending on the exact method of synthesis. However when imaged by TEM the particles were considerably smaller, showing that they most likely exist as clusters of several particles when in dispersion. The particles were nearly monocrystalline and showed magnetic properties on par with published literature. Silica coating gave greater stability to the particles but the thickness of the silica shell proved difficult to control. Regardless of that the encapsulation of the cores was proven by TEM. The fluorescent dye Rhodamine B was conjugated to the linker molecule APTES through EDAC/NHS coupling chemistry. Attempts were made to condense the linker molecule on the surface of the silica shell but major aggregates of APTES were visible in the dispersion of nanoparticles.

Contents

1	Introduction	1
1.1	Clinical motivation	1
1.2	Drug targeting	2
1.2.1	Organic drug carriers	2
1.2.2	Inorganic drug carriers	3
1.2.3	In-Vivo barriers	3
1.3	The Blood Brain Barrier	6
1.3.1	Transport through the BBB	7
1.3.2	Other access points to the CNS	8
1.4	Magnetic nanoparticles	9
1.4.1	Iron oxide Particles	9
1.4.2	Synthesis of Iron oxide particles	10
1.4.3	Functionalization strategies	13
1.4.4	Drug Delivery strategies	14
1.5	Magnetism	16
1.5.1	Magnetic fields	16
1.5.2	The magnetic moment	17
1.5.3	Magnetization and domains	18
1.5.4	Finite size effects in Magnetic nanoparticles	21
1.5.5	The magnetic force and magnetic focusing	23
2	Materials and methods	26
2.1	Materials	26
2.2	Methods	27
2.2.1	Synthesis of Iron oxide particles	27
2.2.2	Silica coating	28
2.2.3	Functionalization	28
2.2.4	Characterization	29
3	Results	31
3.1	Synthesis of magnetic iron cores	31
3.1.1	Co-precipitation	31
3.1.2	Thermal decomposition	38
3.1.3	Summary of IONP synthesis	39
3.2	Silica coating	40
3.3	Rhodamine B conjugation	44

4 Discussion	47
4.1 Iron core synthesis	47
4.1.1 Co-precipitation	47
4.1.2 Thermal decomposition	49
4.2 Silica coating	51
4.3 Rhodamine B conjugation	52
5 Conclusion	53
Bibliography	54
6 Appendix	59

1.1 Clinical motivation

There exists a great need to target drugs more effectively to select location or specific cell types and tissues in the body such as the central nervous system. Treatments for many diseases are plagued by the fact that only a fraction of the administered drug actually reaches the location where it is needed, such as a tumor. Since many drugs can be toxic or are harmful to the cells in the body this limits their usefulness in treatment.

Cancer is an umbrella term used for a myriad of diseases that have the same phenotype defined by out of control cell growth and multiplication. In developed countries cancer is the leading cause of mortality under 70 years and is predicted to increase dramatically due to the aging of the worlds population and an increase in the prevalence of risk factors related to cancer [1]. Cancer cells can spread throughout the body and form multiple tumors in a process called metastasis. It is usually this process and the subsequent growth of multiple tumors that leads to the death of cancer patients. This emphasizes the need to effectively target and destroy cancer cells as soon as they are detected. The treatment of cancers usually combines multiple drugs that inhibit cell growth or promote cell death in chemotherapy cocktails. These treatments are typically plagued by off targeting with the drugs primarily harming the healthy cells of the body. The dosage of these cocktails is not selected for how much is needed to destroy tumors but rather how much the patient can survive [2].

Drug targeting to the central nervous system(CNS) has historically proven difficult. Primarily this is caused by the presence of the blood brain barrier(BBB) which protects the highly sensitive nervous tissue from possible pathogens in the bloodstream. Diseases of the CNS cause approximately 12% of yearly deaths worldwide with cerebrovascular diseases contributing the largest part of those deaths. As with cancers, CNS disease prevalence is predicted to increase dramatically with the worlds aging population [3].

1.2 Drug targeting

Targeted drug delivery is a term used to describe the transport of drugs to specific locations or cell types in the body, causing them to have a higher concentration in these locations relative to others. This is often achieved through the use of drug delivery vehicles. The development of these vehicles has largely been driven by the burgeoning field of nanotechnology which is often defined as the research and development at the atomic, molecular or macromolecular level. This is typically at the length scale of one to a few hundred nanometers. The goal of this research is to provide a fundamental understanding of phenomena and materials at the nanoscale and to create and use structures, devices and systems that have novel properties due to their size. Fabricated nano-sized devices or drug carriers provide various advantages for effective drug delivery. They can carry poorly soluble, unstable or toxic drugs, keeping them from interacting with the cells of the body until they are at their target. This can in theory solve the problems of low blood circulation times, rapid metabolization, off targeting and dangerous side effects [4].

Targeted drug delivery can be either active or passive. Active targeting refers to the use of tissue or cell specific targeting ligands to guide the therapeutic agent to its destination. Passive targeting refers to having the delivery systems passively reach its target e.g. by diffusion in the blood stream or by injecting the particles into the target tissue or organ. These devices can be engineered to undergo rapid changes, conformational or chemical in the presence of a stimulus that is present at the target location. These stimuli can be environmental such as pH or external such as heating or magnetic induction. It is highly desirable for a drug carrier to have multiple functions such as imaging properties, stimuli sensitivity, active localization as well as drug carrying. These multifunctional delivery vehicles can greatly increase therapeutic efficiency [5].

Multiple different innovative methods for drug delivery have been investigated and there exists a wide range of nanoscale compounds based on e.g. synthetic polymers, proteins, lipids and nanoparticles that have been employed for drug delivery. These nanocarriers can roughly be grouped into organic and inorganic, depending on the materials used as their building blocks, see figure 1.1.

1.2.1 Organic drug carriers

Liposomes are phospholipid vesicles that have a bilayer lipid membrane similar to that of a biological membrane. They are classified by their size and number of layers. They are an interesting candidate for drug delivery because they have two phases so they can carry both hydrophilic and hydrophobic drugs as well as having a modifiable surface. Polymeric nanoparticles are formed from synthetic (poly lactic acid, polystyrene) and naturally (gelatin, dextran, collagen) occurring polymers. Drugs can be encapsulated

by conjugating or dispersing in the polymer matrix allowing for sustained release. Micelles are spherical or globular colloidal systems that form by the self assembly of amphiphilic block copolymers in aqueous solutions resulting in hydrophobic cores and hydrophilic shells. The core serves as a reservoir for drugs. There also exist protein based nanocarriers such as the naturally occurring protein Albumin. This carrier has high binding capacity for various drugs as well as obvious biocompatibility. Hydrogels are three dimensional polymeric and hydrophilic networks that absorb large amount of water or biological fluids. They are widely used for various applications such as controlled drug release since they can encapsulate macromolecules [6].

1.2.2 Inorganic drug carriers

Dendrimers are highly branched polymers with a layered structure with a central core and numerous terminal groups making them candidates for conjugation chemistry. They are typically small <15nm and are used for imaging and diagnosis. Quantum dots are colloidal fluorescent nanocrystals with high photostability and are excellent contrast agents for imaging and bioassays. Their size usually ranges from 1-10nm and they are called zero dimensional (0D) material. Carbon nanotubes are synthetic one dimensional(1D) nanomaterials made from carbon. The carbon is formed into graphene rings that wrap into hollow tubes. These tubes are e.g. used for photothermal ablation therapy. Two dimensional(2D) layered double hydroxides(LDH) have received a lot of interest for their potential in drug delivery due to their high drug loading efficiency and biocompatibility. LDHs consist of layers of metal ions and interlayer hydrated ions giving multilayer of alternating host layers where drug molecules can be intercalated. There exists a great number of materials used for solid nanoparticles and a multitude of methods to synthesize and functionalize the particles for imaging or drug delivery purposes. Silica nanoparticles have been extensively researched as a drug carrier due to their ability to form mesoporous structures with controllable pore size giving drugs a physical casing protecting them from degradation. Magnetic particles are used clinically for magnetic resonance imaging(MRI) and have received considerable attention for their potential use as drug delivery vehicles due to their intrinsic magnetic properties, see section 1.5 for detailed information on magnetic particles [6, 7].

1.2.3 In-Vivo barriers

The design of a successful drug delivery system requires a great deal of understanding of how the drug carrier interacts with the body's barriers and its intrinsic defense systems. These barriers can restrict the carriers function by blocking their path into their target tissue or organ, by causing physical changes or by a negative host response [8].

The pharmacokinetics of the nanocarriers as well as their cellular uptake and ability to permeate biological barriers are to a great extent related to physiochemical properties

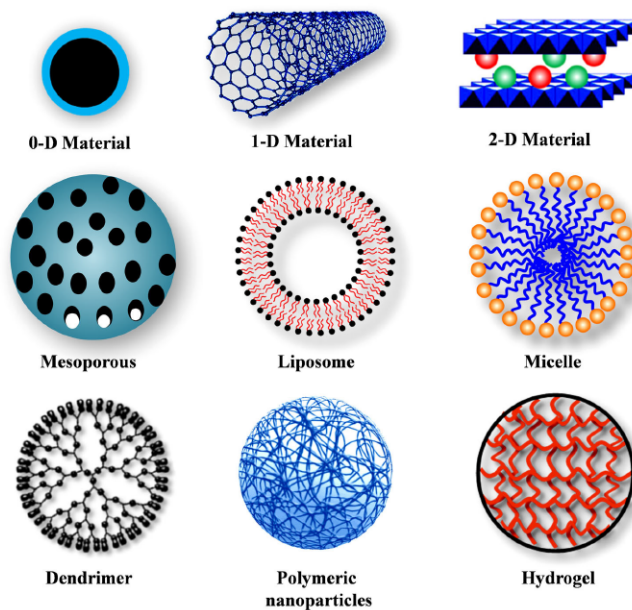


Figure 1.1: Several different types of nanocarriers used for drug delivery. Adapted from [6]

which can to some extent be manipulated. The most important of these properties are size and surface charge as well as other surface properties e.g. hydrophobicity. The size of particles is a key factor whether or not they will be successful in delivery through the blood. The size is a deciding factor on the carriers clearance from the blood and it dictates their permeability from the vasculature as well as their concentration profiles. Particles smaller than 10nm are quickly cleared renally and by extravasation. While particles bigger than 200nm are known to accumulate in the liver, spleen and bone marrow, giving a narrow window for the size range of nanocarriers [9].

Blood is an immensely complex fluid made up of multiple components such as red blood cells, monocytes, platelets, proteins and more. It has a complex interaction with nanocarriers. Highly charged and hydrophobic particles have short circulation times and are quickly opsonized through the adsorption of plasma proteins which leads to their clearance [10]. In short, opsonization is the binding of blood serum components such as serum albumin and immunoglobulins that form a protein corona around the particles. Following the protein absorption the NPs are internalized by phagocytosis, primarily by the macrophages of the reticuloendothelial system (RES or MPS), figure 1.2. The phagosome containing the nanocarrier eventually fuses with a lysosome which contains degrading enzymes that seal the fate of most any drug carrier. To limit these interactions scientists have developed particles coated with polymers such as PEG. These particles readily avoid clearance and are called stealth nanoparticles [11].

Even though a drug carrier successfully survives clearance and uptake in the blood stream they are still faced with the challenge of accurately finding their target tissue, cell type

or organ and then crossing the cell membrane at their target location. When in the cell there is yet another challenge since endocytosed particles will be trafficked intracellularly in endosomal compartments. The endosomes are transported to lysosomes where they and their contents are metabolized. However it is possible to engineer particles for endosomal escape. Depending on the final target of the drug the nuclear membrane can pose yet another barrier [8].

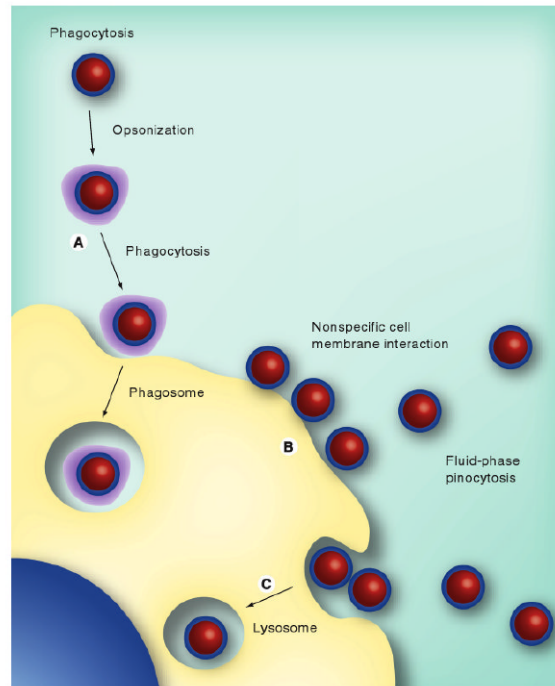


Figure 1.2: The different mechanisms of nanoparticle uptake to the RES. a) Opsonization and phagocytosis, b) nonspecific nanoparticle–cell membrane interactions, c) fluid-phase pinocytosis.[12]

1.3 The Blood Brain Barrier

The blood brain barrier poses a major hurdle for any drug meant to target the brain. The majority of current CNS drugs are small and have the ability to pass the phospholipid membrane of the BBB cells. The BBB is formed by tightly interconnected brain capillary endothelial cells(BCECs). Together with astrocytes, pericytes and neurons they form the impermeable neurovascular unit, figure 1.3. Drug molecules meant to traverse the BBB would need to be lipophilic and small in size as well as being able to avoid or somehow overcome efflux transporters [13].

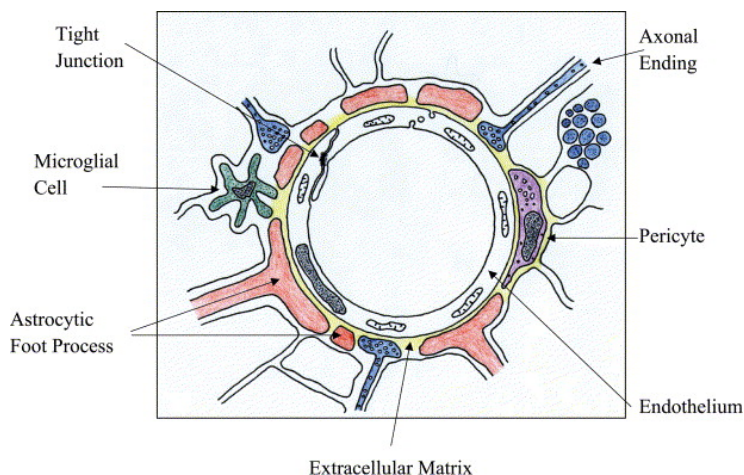


Figure 1.3: A schematic of the neurovascular unit. Adapted from [14]

The BBB poses a physical, enzymatic and efflux barrier between the brain parenchyme and the systemic circulation. The primary part of the actual physical barrier of the neurovascular unit are the BCECs. They do not rapidly exchange molecules between the blood and nervous tissue which minimizes the uptake of extracellular substances. On top of this they have high resistance tight junctions that limit paracellular permeation and adhesion molecules bind them tightly to the extracellular matrix. Pericytes cover large parts of the capillary surface and stabilize the vessel by supporting the BCECs. Finally there are astrocytes who wrap themselves around the BBB and help with maintaing its homeostasis. Together these cells tightly control what passes through the BBB [15]. The BBB has specific transporters for energy chemicals necessary for the function of cells such as glucose, amino acids and more. It also has receptors for receptor mediated endocytosis of cytokines and neurotrophic factors [16]. To further restrict the passage of potential drugs into the brain there exists a barrier of metabolizing enzymes. They generally have high expression in the cerebral vessels and co-localize with efflux pumps. The aforementioned efflux transporters pose yet another challenge for prospective drugs. Several different types of efflux transporters are present on both sides of the BCECs, clearing out metabolites and catabolites from the brain. These functions of the BBB are critical to the homeostasis of the body, and it is known that its breakdown or abnormal function has a role in many pathologies, such as epilepsy [15].

1.3.1 Transport through the BBB

The absorption of molecules across the BBB can occur by active methods like carrier mediated endocytosis, adsorption or receptor mediated transcytosis or passive transport such as paracellular, transcellular, figure 1.4. Due to these formidable barriers the amount of prospective CNS drugs that are able to reach their target in the brain are few and far between. However the use of nano carriers opens up a whole new dimension when it come to delivering drugs to the CNS. There are multiple different strategies that have been developed or theorized for nanoparticles passing the BBB. A particle can pass through the tight junctions or cause toxic local effect on the barrier, increasing permability. They can pass through by transcytosis or by endocytosis and then releasing the drug for subsequent exocytosis. Or any combination of the above.

Research has shown that trans- and endocytosis are the most common routes. With a good understanding of the receptor mediated and adsorption transcytosis mechanisms we can better engineer particles able to pass through the BBB. Receptor mediated transcytosis of NPs is based on the reciprocal action of a ligand bound to the particle and it's corresponding receptor. Following this there can form an endocytic vesicle. This leads to the transcytosis of the particle encapsulated in the vesicle [17].

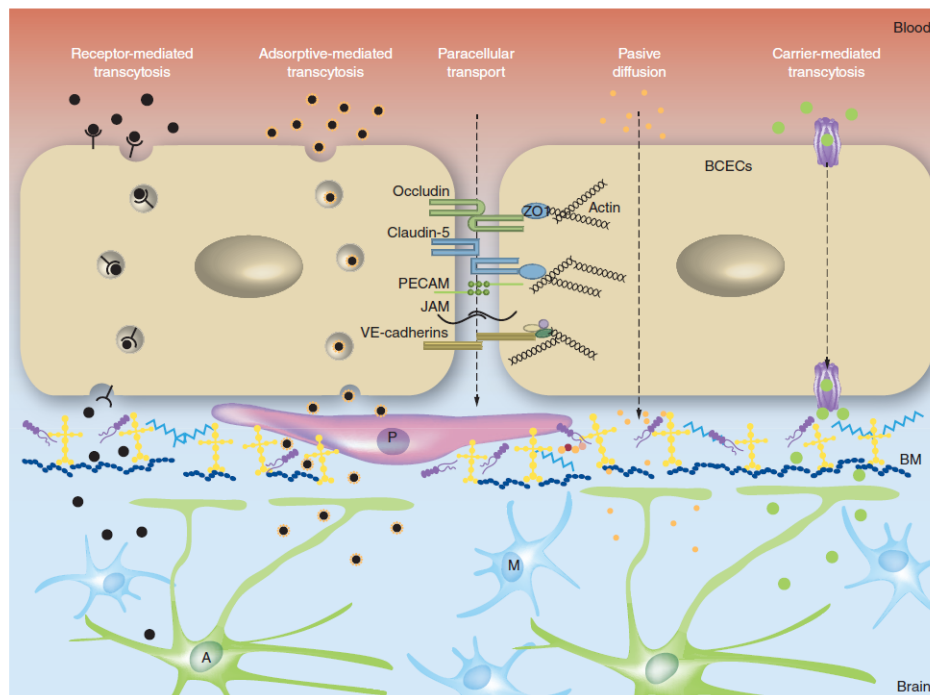


Figure 1.4: The different mechanisms molecules use to cross the BBB. [18]

1.3.2 Other access points to the CNS

There are two other barriers to the CNS , the olfactory bulb which is the only externally exposed part of the CNS and the blood-cerebrospinal fluid barrier. Nasal delivery to the brain has been investigated for a variety of drugs but the delivery faces many of the same problems seen in the BBB such as low membrane permeability and the possibility of enzymatic degradation [19]. As well as the limited surface of the olfactory bulb making it harder to delivery an effective amount of drugs [16]. Delivery through the CSF on the other hand is plagued by the fact that the entire volume of the CSF is turned over approximately every 5 hours in a human while the rate of diffusion to the brain is minimal [20].

1.4 Magnetic nanoparticles

In recent years magnetic nanoparticles have received an enormous amount of attention from the scientific community for their various uses. In biomedicine their use as MRI contrast agents is already common and there is a large amount of interest in using them as drug delivery vehicles due to their intrinsic ability to be manipulated in vivo by an externally applied magnetic field. This gives a whole new dimension in drug targeting; magnetic targeting, in addition to the previously mentioned active and passive targeting. [21].

Magnetic targeting can guide magnetic drug carriers to select tissues and location in the body using an applied magnetic field. This can aid greatly in preferentially guiding harmful drugs to where they are needed, thereby reducing the harm experienced by a patient in e.g. chemotherapy as well as overcoming difficult barriers such as the BBB [22]. There are however many factors to consider for successfully manipulating nanoparticles in vivo, see section 1.5.5 for a deeper analysis on magnetic targeting.

Due to these intrinsic properties of magnetic nanoparticles they have been investigated for the use in the field of theranostics, simultaneous diagnosis and treatment. In theory it is possible to use these particles for simultaneous drug delivery and imaging with MRI or conjugated fluorescence probes [23].

On top of all these other properties magnetic nanoparticles can themselves be used for treatment by hyperthermia. When magnetic nanoparticles are exposed to an alternating magnetic field they can heat tissues in the body and cause irreversible damage [24].

There exists a multitude of different materials and likewise a large number of methods for the synthesis of magnetic nanoparticles. Cobalt, nickel and iron oxides are commonly used for particle synthesis but for biomedical purposes iron oxide particles are the most common due to their biocompatibility, biodegradability as well as their relative ease of synthesis [22].

1.4.1 Iron oxide Particles

Iron oxides are commonly found in nature and exist in many stable forms, the most common of which are hematite(αFe_2O_3), magnetite(Fe_3O_4) and maghemite(γFe_2O_3). They all have found some use in industry, primarily as catalysts or pigments. Maghemite is found in nature as the weathering product of magnetite and is ferrimagnetic. All of them have some magnetic properties but magnetite shows the strongest magnetism of any transition metal oxide. Magnetite is ferromagnetic at room temperature and has a Curie temperature of 850K [25]. Magnetite is not particularly stable under ambient conditions and can oxidize to maghemite. It can also be done on purpose, giving less magnetic but more chemically stable particles [26].

1.4.2 Synthesis of Iron oxide particles

As was mentioned previously there exists a multitude of methods to synthesize magnetic iron oxide particles. These methods vary in complexity and difficulty and give different results with regards to control of size, polydispersity and colloidal stability. Since these factors are highly important for the properties and behaviours of nanocrystals their control is very important for the successful use of the particles. Regardless of whether or not it is for complex biomedical purposes or inkjet printing.

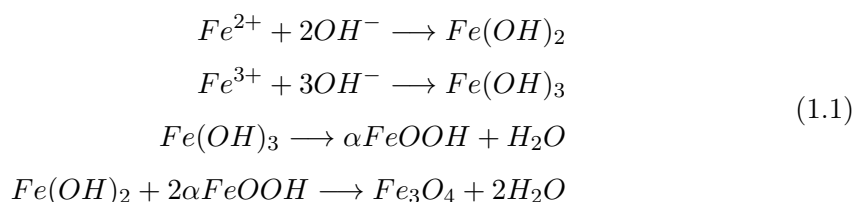
An ideal synthesis gives the desired size of monodisperse magnetic grains for a specific purpose in a scalable and reproducible process. The number of methods and their corresponding literature far exceeds the scope of this thesis but there are two methods that stand out as most commonly used and they will be further elaborated on. They are thermal decomposition and co-precipitation, figure 1.5. For further details on other methods see [21] and [26].

Synthetic method	Synthesis	Reaction temp. [°C]	Reaction period	Solvent	Surface-capping agents	Size distribution	Shape control	Yield
co-precipitation	very simple, ambient conditions	20–90	minutes	water	needed, added during or after reaction	relatively narrow	not good	high/scalable
thermal decomposition	complicated, inert atmosphere	100–320	hours–days	organic compound	needed, added during reaction	very narrow	very good	high/scalable
microemulsion	complicated, ambient conditions	20–50	hours	organic compound	needed, added during reaction	relatively narrow	good	low
hydrothermal synthesis	simple, high pressure	220	hours ca. days	water-ethanol	needed, added during reaction	very narrow	very good	medium

Figure 1.5: A comparison of methods used to synthesize magnetic nanoparticles. Adapted from [26]

Co-Precipitation

Co-precipitation is the simplest and possibly the most efficient method to produce iron oxide nanoparticles, see figure 1.6. The method is based on the base catalyzed co-precipitation (equation 1.1) of a stoichiometric mixture of Ferrous and Ferric salts, typically at 2:1 Ferric to Ferrous ratio in an aqueous medium. The method allows for organic solvent free synthesis at ambient conditions. Under basic conditions the iron salts form ferrous hydroxide, $Fe(OH)_2$ and Goethite, $\alpha FeOOH$, that coprecipitate as precursors to nanoparticle formation [27].



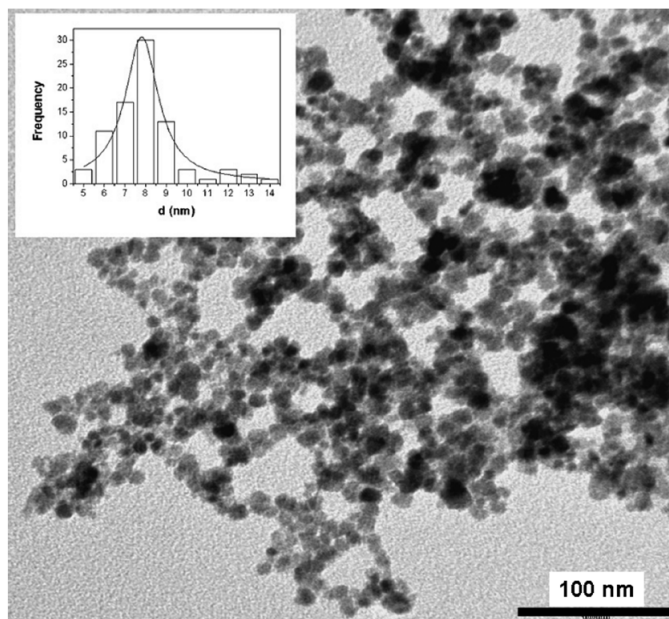


Figure 1.6: TEM image of iron oxide nanoparticles synthesized by co-precipitation. Insert: Size histogram. Adapted from [22].

Two stages are involved in the nanoparticle formation. At first a rapid, short burst nucleation followed by a slow growth of nuclei by diffusion of solutes and smaller particles to the crystal structure. This nucleation and subsequent growth are described by the classical mechanisms of Lamer supersaturation [17], and Ostwald ripening. The Lamer diagram illustrates this process. In a supersaturated solution the nuclei grow at a similar speed giving a narrow size distribution [28, 29].

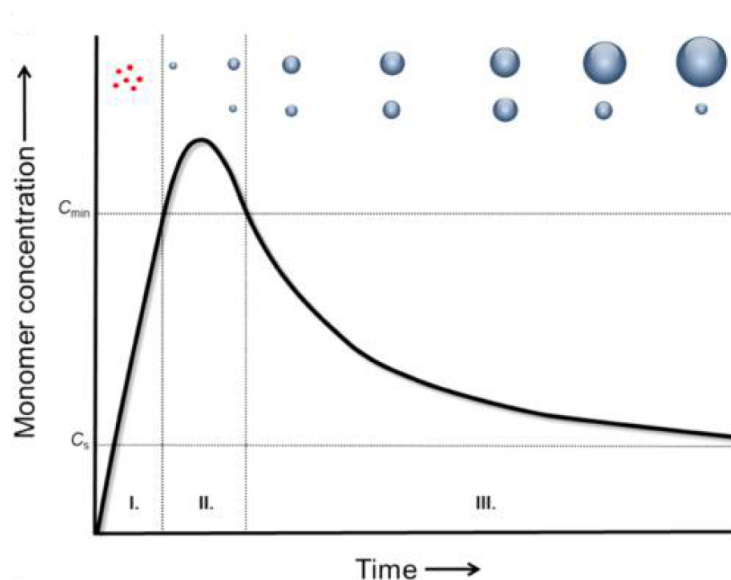


Figure 1.7: The three stages of classical Lamer supersaturation mechanism. [28].

One of the main problems with co precipitation is low crystallinity which in turn gives

poorer magnetic properties. There are several strategies that have been investigated to increase the crystallinity such as the addition of co-anions like sulfate and lactate which have been shown to interact with the precursors to nanoparticle formation. Varying the ratios of Ferrous and Ferric ions has also been shown to increase crystallite size [27]. The presence of oxygen is known to induce the oxidation of magnetite to maghemite so the reaction is typically kept under anaerobic conditions [21]. The upper limit in size for coprecipitation seems to be around 50nm particles and there are many factors that influence the size such as pH, stirring rate, presence of salts, nature of surfactant and more [22].

Thermal Decomposition

A considerably more difficult method than coprecipitation mentioned above; thermal decomposition is based on the decomposition of organometallic precursors to form smaller, highly crystalline magnetic iron oxide nanocrystals. Typically this is done in high temperature solvents such as 1-hexadecene, octyl ether and 1-octadecene. This method allows for good control of size (upwards of 50nm) and shape by varying the precursor and reaction conditions, see figure 1.8 [26].

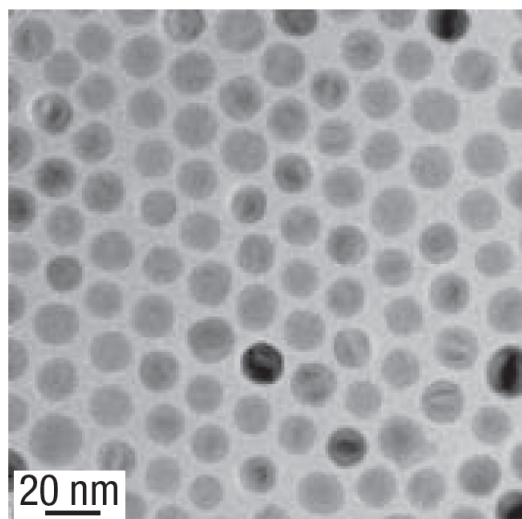


Figure 1.8: Iron oxide nanoparticles synthesized using thermal decomposition. Adapted from [30]

Examples of organometallic precursors are iron oleate, iron pentacarbonyl and iron oxylhydroxide. Larger amounts of excess surfactant are known to alter the reaction kinetics, resulting in larger particles with a broader size distribution. Particles produced from these precursors are dispersible in organic solvents such as chloroform and hexane and would require further modification for aqueous or biological purposes [31].

There are however more factors to consider than just size and polydispersity such as the all important magnetic properties. Thermal decomposition (and magnetic nanoparticle synthesis in general for the matter) often yields particles with poorer than expected

magnetic properties. This is to some extent caused by a magnetic dead layer, found on the surface of the particles. This layer contains oxidized iron which contributes to the disorder of the magnetic dipoles [32].

1.4.3 Functionalization strategies

Nanoparticles have a proportionally high surface area to their volume and magnetic nanoparticles are no exception. The surface of iron particles is reactive to oxidation, which results in a less magnetic particle. Therefore the protection of magnetic iron cores is important to obtain a physically and chemically stable colloidal system [22].

The physical stability of colloids is the result of a complex equilibrium of attractive and dispersive forces. The attractive forces are generally short range and are called the Van der Waals forces. The dispersive force is longer range and caused by electrostatic repulsion. The interplay of these forces is called the DLVO theory. For magnetic nanoparticles the magnetic dipolar forces have to be accounted for. These interactions are anisotropic but are globally attractive when the interparticle potential is integrated over all directions. Finally, there are steric interactions. These forces are most common in particles that have been modified with polymers. With an understanding of what forces are at play in colloidal stability we can better understand how to engineer particles for a stable system.

For a stable suspension, iron oxide nanoparticles are typically coated with stabilizers such as citrate or oleic acid. These molecules are called monomeric stabilizers and typically give the particle greater charge or act as steric stabilizers, preventing aggregation. The choice of surfactant can be tailored for dispersibility in either aqueous or organic solvents. For example, citrate coated particles are dispersible in water but oleic acid coated particles in chloroform, hexane, etc [21].

Although the monomeric stabilizers help to prevent the aggregation of the iron cores in dispersion, more protection is often required for chemical stability. Multiple inorganic materials like silica and gold have been used to coat the magnetic cores, forming a core-shell structure. These coating not only offer a highly chemically inert shell to protect the core but are themselves a platform for further modification. Examples of this are the binding of targeting ligands, fluorescent molecules or for stabilizing polymers. Both gold and silica are themselves used to make nanoparticles and there exists a rich literature for their functionalization.

Electrostatic stabilization is rarely enough to prevent aggregation in high salt environments such as in biological fluids. Polymeric stabilizers can offer greater stability through steric repulsion. Most commonly, dextran, carboxydextran, starch, glycoaminoglycan, PEG and PVA are used. As mentioned in section 1.2.3, polymers can also prevent nanoparticle uptake by the RES, increasing blood circulation time.

Liposomes and micelles are also used to encapsulate magnetic particles. Their in vivo

behaviour is well established and they are known to have long circulation times when properly modified. A liposome can encapsulate multiple iron cores as well as a drug payload. See figure 1.9 for an overview of particle coatings [33].

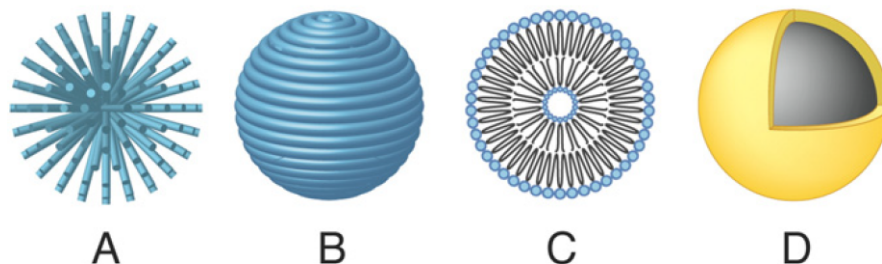


Figure 1.9: Different coating methods typically used for magnetic nanoparticles. A) End grafted polymer, B) Fully encapsulated in polymer, C) Liposome encapsulated, D) Core shell . Adapted from [33]

1.4.4 Drug Delivery strategies

Multiple different strategies have been employed to use magnetic nanoparticles as drug delivery vehicles. Since most iron cores are coated with either polymers or inorganic materials it is highly desirable if the coating can also serve as a capsule for the drug. Drug payload and release rate are important parameters and drug loading by surface adsorption is often insufficient to reach therapeutic concentrations so encapsulation is more often employed [22].

Silica coated magnetic nanoparticles are a popular choice for drug delivery systems. Silica nanoparticles have received a lot of interest lately in drug delivery nanotechnology due to their ease of synthesis, surface conjugation and their controllable porosity [34]. These qualities of silica still apply when coated on magnetic nanoparticles and there exists a multitude of articles that show the use of silica coated particles to make drug delivery systems. For example Badruddoza et al created a multifunctional particle that was fluorescent, contained a targeting ligand as well as drug carrying abilities through β -Cyclodextrin, see figure 1.10 [35].

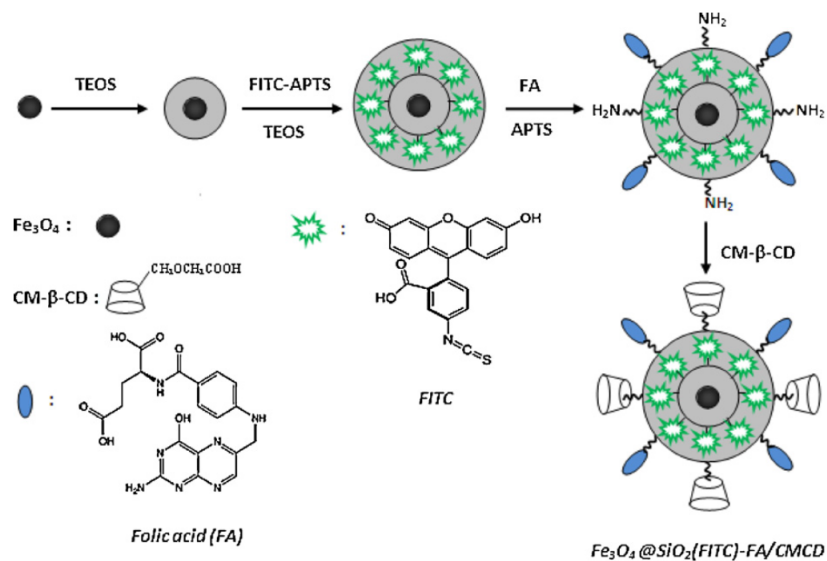


Figure 1.10: A schematic of the synthesis of a multifunctional magnetic nanoparticle. Adapted from [35]

The pores in silica can be used to carry molecules such as drugs. Researchers have even been able to engineer removable caps that ensure the cargo does not leak out [36]. It has also been shown to be possible to use thermoresponsive polymers on the surface of porous silica coated particles that act as gatekeepers for encapsulated drugs. The particle can then be heated through an alternating magnetic field, giving a remotely controlled release of cargo [37].

1.5 Magnetism

1.5.1 Magnetic fields

All magnetic phenomena are due to charges in motion. A current passing through a wire produces a magnetic field around it see figure 1.11. Magnetic field strength is measured in Amperes per meter (A/m). For example, a circular loop of conductive material with a radius of 1 meter carrying a current of 1 ampere produces a field \mathbf{H} of strength 1 A/m see equation 1.2. Magnetic field strength is often confused with the flux density \mathbf{B} , which is closely related to the field strength but also depends on the material within the field. Flux density is simply the total magnetic flux divided by the area through which it flows [38]. The flux density is arguably better to describe the strength of a magnetic field so there is some contention as to which field should be called the magnetic field. Therefore some modern authors prefer to simply name the fields \mathbf{B} field and \mathbf{H} field respectively [39].

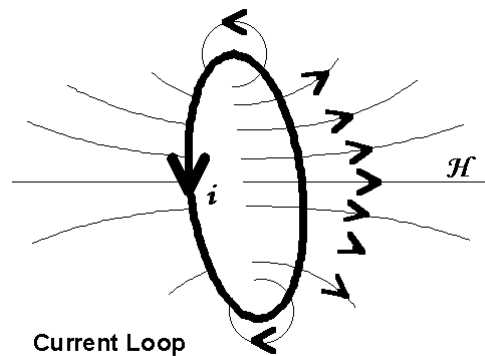


Figure 1.11: A current loop producing a magnetic field. Adapted from [40]

$$H = I/2r \quad (1.2)$$

The magnetic flux density of a magnetized material depends on the applied magnetic field and the magnetization of the material. It has the unit Tesla see equation 1.3.

$$\mathbf{B} = \mu_0(\mathbf{H} + \mathbf{M}) = \mu_0(1 + \chi_m)\mathbf{H} \quad (1.3)$$

Where χ_m is the magnetic susceptibility (see section 1.5.3) , μ_0 is the permeability of free space.

For the case of a dilute suspension of particles in water the magnetic susceptibility can be assumed to be effectively zero. Therefore the B field is simply proportional to the H field. 1.4 [41].

$$\mathbf{B} = \mu_0 \mathbf{H} \quad (1.4)$$

1.5.2 The magnetic moment

The most fundamental element in magnetism is the magnetic moment. Often imagined as a pair of closely spaced dipoles analogous to electric dipoles. This is however misleading since there is no such thing as a single north or south pole on a magnet. Magnetism is not due to monopoles but rather moving electrical charges. Therefore it is more accurate to think of magnetic dipoles as tiny current loops. This is known as the Amperian model, see figure 1.12.[39]

The magnetic moment is the starting point when discussing the behaviour of magnetic material within a field. A magnetic moment such as the one from a current loop experiences torque when placed in a magnetic field. This aligns it's axis along the direction of the field, much like a compass needle. This torque increases with the strength of the moment. This means that the moment of a magnet is a measure of its ability to produce and be affected by a magnetic field. [38]

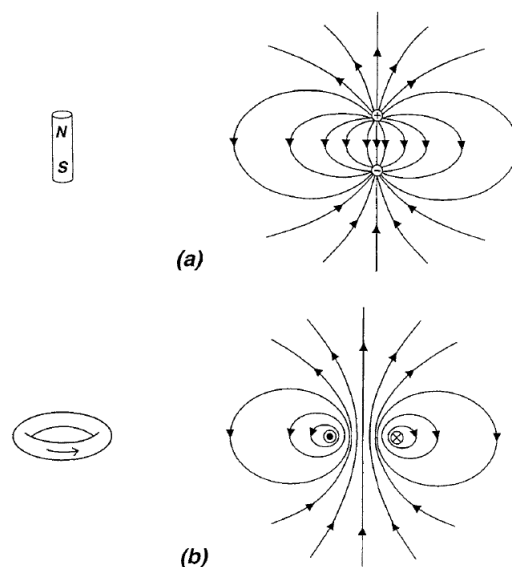


Figure 1.12: Magnetic dipoles. a)Magnetic charge model b) Ampere model. Adapted from [38]

A current loop has a magnetic moment associated with it, the magnitude of which can be found from the area of the loop see equation 1.5.

$$m = I \cdot \text{area} \quad (1.5)$$

1.5.3 Magnetization and domains

On the atomic scale, magnetic material can be imagined to have tiny "current loops", electrons orbiting around nuclei. For macroscopic purposes these currents are so small that they are treated simply as magnetic moments. Ordinarily the random orientation of these atoms and their magnetic dipoles causes them to effectively cancel each other out. But when an external magnetic field is applied the moments can form a net alignment and the material can be said to be magnetized, that is the medium as a whole is magnetically polarized. We describe the state of magnetic polarization by a vector quantity called simply the magnetization or \mathbf{M} . The magnetization is the vector sum of all the magnetic moments of the atoms in the material per unit volume of the material, see equation 1.6. [25] [39]

$$\mathbf{M} \equiv \frac{\Sigma m}{V} \text{ magnetic dipole per unit volume} \quad (1.6)$$

Not all materials respond the same way to an external magnetic field. Some materials gain a magnetization parallel to the magnetic field and are called paramagnetic while some materials gain magnetization opposite to the field and are called diamagnetic. Diamagnetism is seen in material with filled electron sublevels with paired magnetic moments. Paramagnetism on the other hand is caused by uncoupled atomic moments [42]. Ferromagnetic materials differ from the other two because they require no external fields to sustain their magnetization. Ferromagnetism is what is typically thought of as "magnetism", as seen in compass needles and household magnets. As in paramagnetism the magnetic dipoles are associated with the spins of unpaired electrons. Iron, the most common ferromagnetic material has a particularly strong magnetic moment due to the fact that an iron atom contains four unpaired electrons in its $3d$ orbitals.

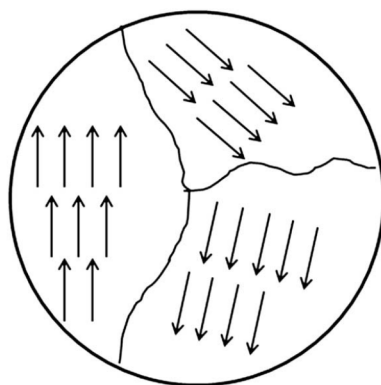


Figure 1.13: Magnetic domains in a bulk material. Adapted from [25]

In a ferromagnet the dipoles preferentially point in the same direction as their neighbours see figure 1.13. This alignment is however limited to relatively small patches of the material called domains. Each domain can contain millions and billions of dipoles with

the same direction of magnetization. The domain alignment in a ferromagnetic crystal can take several forms, figure 1.14. A typical ferromagnetic crystal has moments aligning in the same direction but a ferrimagnetic crystal has two types of moments aligning in an antiparallel fashion. If these magnetic moments are of the same magnitude then the crystal is antiferromagnetic and has no net magnetic moment.

It may seem surprising that not all iron materials are magnetic this is because any sizeable amount of material e.g. a nail contains an enormous amount of domains with their own magnetic field that cancel each other out. However a permanent magnet can be made by introducing a piece of ferromagnetic material to a strong magnetic field. The torque experienced by the dipoles tends to align the domains parallel to the field until one domain takes over entirely. When the field is switched off some of the domains return to a randomly oriented state but there should remain a high number of domains still aligned together, giving a net magnetization.

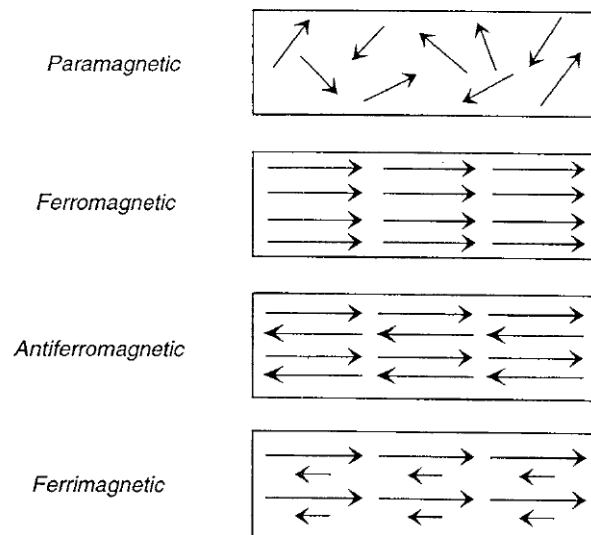


Figure 1.14: Moment alignment in different types of materials. Adapted from [38]

As mentioned before the magnetization of paramagnetic and diamagnetic materials is sustained by a magnetic field and for most substances the magnetization is proportional to the field. Provided the field is not too strong see equation 1.7

$$\mathbf{M} = \chi_m \mathbf{H} \quad (1.7)$$

Where χ is constant of proportionality called magnetic susceptibility. This value is different for materials and has a negative value for diamagnets. It is however misleading to assign magnetic susceptibility to a ferromagnet since they refer to the differential increase of \mathbf{H} and the resulting differential change in \mathbf{M} , they are not constants but functions of \mathbf{H} .

Logically, ferromagnetic materials reach a peak magnetization (Where all the domains are aligned) in a strong enough field and are then said to be saturated see figure 1.15 (b). However if the field is then reduced to zero, some magnetization remains giving a permanent magnet (c). As mentioned before this is due to the magnetic domains having a net alignment giving a permanent magnetization. If the magnetic field is then applied in the reverse direction the magnetization will go to zero (e), and then the domains are fully aligned and the ferromagnet is once again saturated only in the opposite direction. Another important parameter is the coercive field seen at points (g) and (d). This represents the field necessary to completely demagnetize the sample. This parameter is important for materials that are subjected to cycles of magnetizations such as recording media [43] [39].

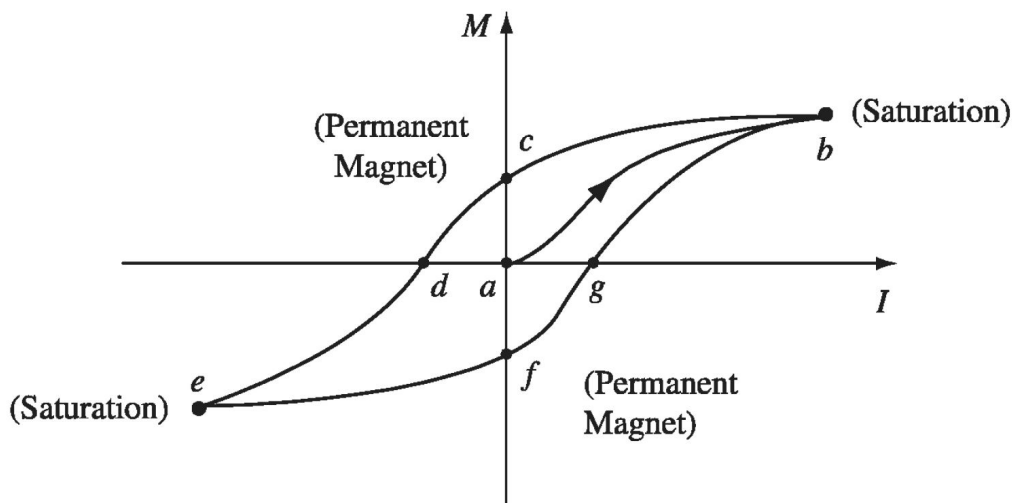


Figure 1.15: The hysteresis loop of a ferromagnetic material. a) Non magnetized, randomly oriented domains. b) and e) Saturated, fully aligned domains. c) and f) Remnant magnetization, some aligned domains. d) and g) The coercive field, [39]

1.5.4 Finite size effects in Magnetic nanoparticles

Magnetic nanoparticles exhibit some interesting finite-size effects, primarily single domain behaviour and superparamagnetism [44]. As mentioned before bulk ferromagnetic materials consist of multiple domains of aligned dipoles, however if we go from bulk material to a nanoparticle we will eventually cross a critical threshold where it is more energetically favorable to have a single domain state. In this state the entire particle is uniformly magnetized and all the spins will be aligned in the same direction [26].

In multidomain structures the actual formation of domain walls is driven by the balance of magnetostatic energy and the domain wall energy. At the point where a bulk material consists of a single domain, the energy needed to create a domain wall is greater than the energy it takes to support the external magnetostatic energy of the single domain state. The critical diameter for a single domain state usually lies in the range of a few tens of nanometers to a few hundred. See equation 1.8 for the critical diameter equation for a spherical particle [45].

$$D_{cr} = 72 \frac{\sqrt{AK}}{\mu_0 M_s^2} \quad (1.8)$$

Where D_{cr} is the single domain critical diameter, K is the anisotropy constant, A the exchange stiffness constant, μ_0 the vacuum magnetic permeability and M_s the saturation magnetisation.

The anisotropy energy KV , separates the two energetically equivalent directions of magnetization in a single domain particle. But with decreasing particles size the thermal energy starts to exceed this energy barrier $k_B T > KV$. This causes the magnetization to flip easily and the particle now is said to be superparamagnetic. The relaxation time of the moment can be found using equation 1.9. If the relaxation time of the particle is shorter than the measuring time (usually in the range of nanoseconds) then the spontaneous magnetization is zero and the particles can be said to be superparamagnetic. Superparamagnetic particles show no hysteresis loop when their magnetization is measured since they have no coercivity, see figure 1.16.[45] [46]

$$\tau = \tau_0 \exp\left(\frac{KV}{k_B T}\right) \quad (1.9)$$

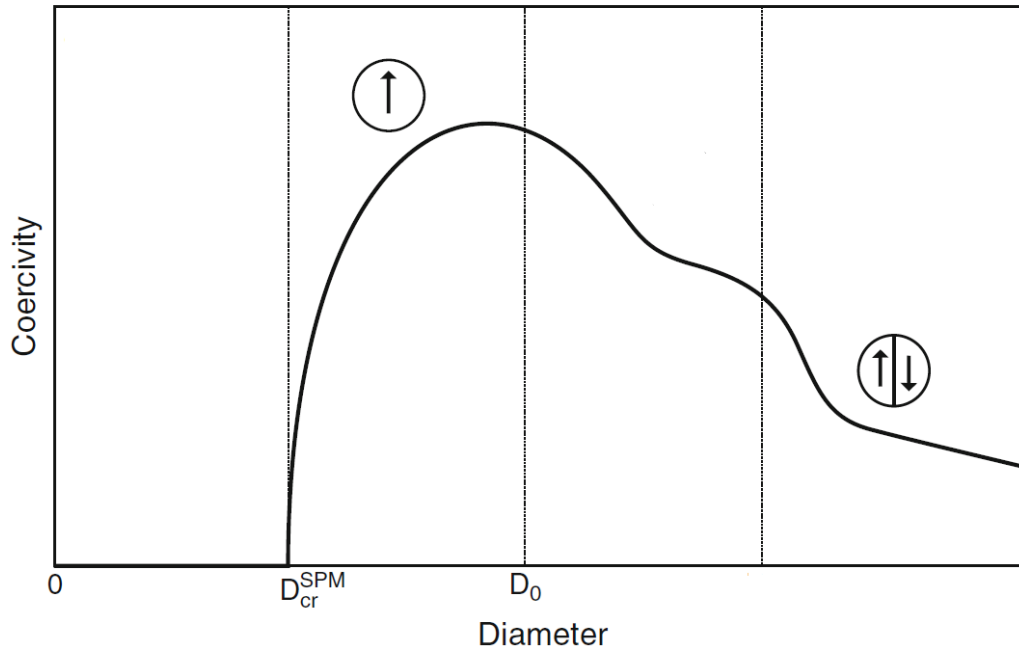


Figure 1.16: Coercivity plotted against size. D_{spm} is the critical diameter for superparamagnetism and D_0 the critical single domain diameter. Adapted from [45]

The magnetization of a system of superparamagnetic nanoparticles can be approximated using the Langevin paramagnetic equation 1.10. This equation allows for the extraction of the individual magnetic moment per particle from a measured experimental isothermal magnetisation curve, see figure 1.17. Care must be taken not to apply the equation to highly anisotropic particles or neglecting the presence of interparticle interactions [43].

$$M_{spm} = N_{spm} \mu_{spm} \left[\coth \left(\frac{\mu_0 \mu_{spm} H}{k_B T} \right) - \frac{k_B T}{\mu_0 \mu_{spm} H} \right] \quad (1.10)$$

Where N_{spm} is the number of superparamagnetic particles with an average moment μ_{spm} .

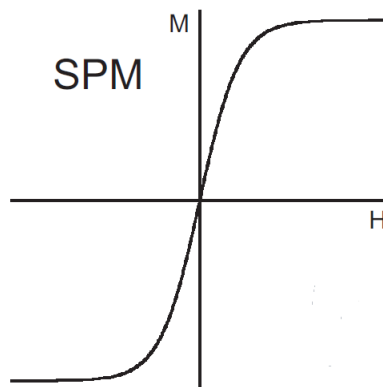


Figure 1.17: The magnetization curve of a superparamagnetic nanoparticle. Adapted from [41]

1.5.5 The magnetic force and magnetic focusing

Magnetic nanoparticles offer a great opportunity for focused targeting of possibly harmful drugs to select regions in the body and there exist a large number of articles displaying their use for this [18, 35, 47–50] . However most articles do not present a solid theoretical foundation for in vivo magnetic targeting which could answer why highly similar experiments fail while others succeed. This section aims to answer some of the key questions concerning in vivo magnetic targeting such as what factors/magnetic design parameters need to be known to make a case that focusing is even possible for select locations in the body.

There are two primary forces acting on a magnetic nanoparticles in a blood vessel, figure 1.18, the fluidic force and the magnetic force(when an applied magnetic field is present). The motion of these particles can be described with newtons law 1.11.

$$m_p \frac{dv_p}{dt} = F_{mag} + F_{fluidic} \quad (1.11)$$

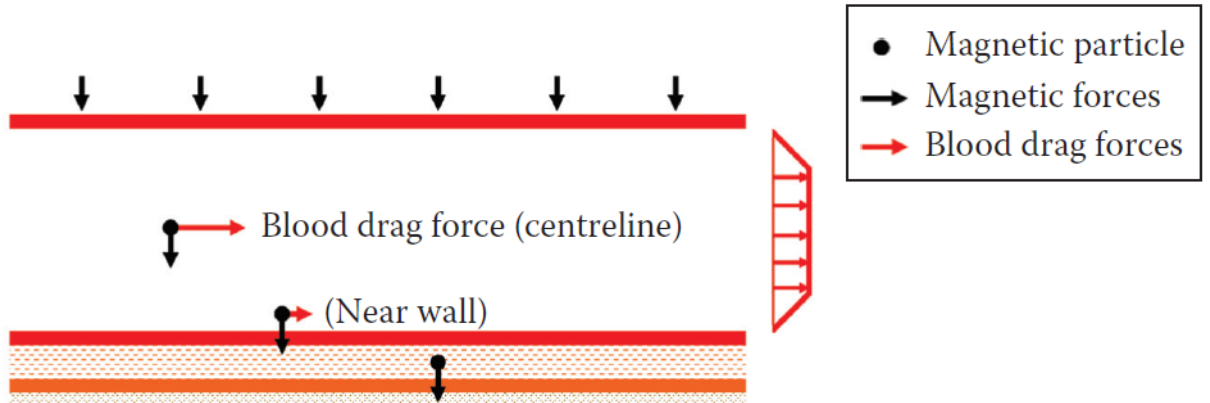


Figure 1.18: A schematic of a magnetic nanoparticle in a blood vessel and the forces it experiences. Adapted from [51]

The force acting on a magnetic particle in a magnetic field is usually found by treating them as a point like magnetic dipole \mathbf{m} and is approximated by equation 1.12

$$F_{mag} = (m \cdot \nabla)\mathbf{B} \quad (1.12)$$

This equation can be further developed by replacing the magnetic moment and the \mathbf{B} field with equations 1.6 and 1.4 respectively[41].

$$F_{mag} = \mu_0 V_m (\mathbf{M} \cdot \nabla)\mathbf{H}_a \quad (1.13)$$

Here μ_0 is the permeability of free space, V_m is the volume of the particle, \mathbf{M} is the magnetization of the particle and \mathbf{H}_a is the strength of the applied magnetic field. The magnetization can be replaced with equation 1.7 For the special case of spherical particles the magnetization can be expressed as equation 1.14 [38] [52]..

$$\mathbf{M} = \frac{3\chi}{(\chi + 3)} \mathbf{H}_a \quad (1.14)$$

The equation then becomes:

$$F_{mag} = \frac{4\pi r^3}{3} \mu_0 \frac{3\chi}{(\chi + 3)} (\mathbf{H}_a \cdot \nabla) \mathbf{H}_a = \frac{2\pi r^3}{3} \mu_0 \frac{\chi}{(\frac{1}{3}\chi + 1)} \nabla(\mathbf{H}_a^2) \quad (1.15)$$

Here r is simply the radius of the nanoparticle. The first relation clearly shows that a spatially varying field ($\mathbf{H}_a \cdot \nabla \neq 0$) is needed to produce a magnetic force The second relation states that a magnetic force on a paramagnetic particle is always from a low to high magnetic field and proportional to the gradient of the magnetic field strength/intensity squared [53].

If we consider a volume of ferrofluid entering in a magnetic field we can expect it to be strongly magnetized. If we neglect interparticle interactions and assume sufficient anti-oxidation coatings we can calculate the force on a volume of ferrofluid with equation 1.16

$$F_{mag} = \frac{2\pi r^3}{3} \mu_0 \frac{\chi}{(\frac{1}{3}\chi + 1)} C \nabla(\mathbf{H}_a^2) \quad (1.16)$$

Where C is the concentration of the particles [*number/m³*]

The forces acting on a particle in blood

A magnetic particle in flowing blood will accelerate in the direction of the previously mentioned magnetic force until it reaches an equilibrium velocity with the surrounding blood. The opposing force caused by stokes drag on a spherical particle is described by equation 1.17.

$$F_s = 6\pi r \eta v_R \quad (1.17)$$

Where η is the dynamic viscosity and v_R is the relative velocity.

When the stokes drag force equals the applied magnetic force the particle has reached equilibrium velocity. And we can now define the magnetic drift coefficient k .

$$F_s = F_{mag} \quad (1.18)$$

$$v_R = \frac{a^2}{9\eta} \mu_0 \frac{\chi}{(\frac{1}{3}\chi + 1)} \nabla(\mathbf{H}_a^2) = k \nabla(\mathbf{H}_a^2) \quad (1.19)$$

Where $k = \frac{a^2}{9\eta} \mu_0 \frac{\chi}{(\frac{1}{3}\chi + 1)}$

Blood flow is an interesting case of non Newtonian liquid due to the presence of blood clotting proteins that create aggregates at low shear rates. This means blood has a plug flow profile which can be fit empirically 1.20

$$v_B = v_{Bmax} \left(1 - \left(\frac{r}{R}\right)^\xi\right) \quad (1.20)$$

Where v_B is the blood velocity and ξ is a constant for a particular profile. To fit the experimental data of the cardiac cycle $\xi = 9$ is usually chosen.

The random motion of particles due to thermal fluctuations is described by Brownian motion 1.21

$$D_B = \frac{k_B T}{6\pi\eta r} \quad (1.21)$$

The concentration change of ferrofluid particles is described by their flux. The concentration increases at a location where there is positive flux and decreases where it is negative. The flux can be described as the sum of the previously mentioned terms, that is the blood flow convection, magnetic drift and the diffusion 1.22.

$$\frac{\partial}{\partial t} C(x, y, t) = -\nabla \cdot \left[-D_{tot} \nabla C + C V_B(y) + C k \nabla(H_a^2(x, y)) \right] \quad (1.22)$$

If we consider a vessel geometry with a constant magnetic force throughout acting only in the negative y direction we can describe the describe the concentration of magnetic particles using the partial differential equation 1.23.[53]

$$C(x, y) = -\nabla \cdot \left[-D_{tot} \nabla C + C(V_{Bmax} [1 - \left(\frac{y}{R}\right)^\xi], 0) + C(0, -k \nabla H_a^2) \right] \quad (1.23)$$

Using these equations in-vivo particle behaviour can be estimated and simulated to evaluate whether or not magnetic targeting is possible with the parameters at hand e.g. the magnetic moment, particle size, blood velocity, magnet strength and it's distance from the blood vessel [43].

Materials and methods 2

The following chapter presents the materials used and descriptions of the methods used in this project.

2.1 Materials

Table 2.1: Information about the materials used in this project.

Chemicals	Cas Nr.	Lot Nr.	Manufacturer
1-Octadecene	112-88-9	MKBD0024	Sigma
3-Aminopropyltriethoxysilane	919-30-2	12915KD-106	Sigma
Ammonium hydroxide	1336-21-6	STBG9817	Sigma
Chloroform	67-66-3	SHBJ2941	Sigma
Disodium phosphate	7782-85-6	056K0113	Sigma
DMSO	67-68-5	250,680,407	Th. Geyer
EDAC	25952-53-8	89H0804	Sigma
Ethanol	64-17-5		VWR chemicals
Hexane	110-54-3	U04624	Sigma
Hydrochloric acid	7647-01-0	SZBG2220	Fluka
Iron(II)chloride tetrahydrate	13478-10-9	H0460	Fluka
Iron(II)sulfate heptahydrate	7782-63-0	TA698265	Merck
Iron(III)chloride hexahydrate	10025-77-1	SZBB1020V	Sigma
Methanol	67-56-1	SHBC9019V	Sigma
Monopotassium phosphate	7778-77-0	SLBR1363V	Sigma
N-Hydroxysuccinimid	6066-82-6	456427/1	Fluka
Oleic acid	112-80-1	70380	Riedel-de Haën
Potassium Chloride	7447-40-7	1121871	Fluka
Rhodamine B	81-88-9	HU01329LN	Aaldrich
Sodium Chloride			
Sodium Hydroxide	1310-73-2	SZBE2520V	Sigma
Sodium Oleate	143-19-1	ZBIC-QC	TCI
Sulfuric acid	7664-93-9	SZBF3430V	Honeywell fluka
Tetraethyl orthosilicate	78-10-4	BCBH4940V	Sigma
Toluene	108-88-3	STBF7647V	Sigma
Trisodium citrate	6132-04-03	28H0209	Sigma

2.2 Methods

2.2.1 Synthesis of Iron oxide particles

Thermal Decomposition

Thermal decomposition was performed with a protocol adapted from [31] and [30].

The iron oleate precursor for nanoparticles synthesis was synthesized by dissolving 20mmol of $FeCl_3$ and 60mmol of Sodium Oleate (1:3) in a mixture of 40mL EtOH, 30mL H_2O , 70mL Hexane (4:3:7). The mixture was then refluxed at 70°C for four hours. The upper organic layer of the solution was then washed three times with approximately 30mL of water. After that the layer was isolated and allowed to dry.

Due to the high price of sodium oleate, a few different ways of performing iron oleate synthesis were evaluated. Firstly oleic acid(66-88%) in liquid form was used instead of sodium oleate. Secondly sodium oleate was synthesized by saponification of the oleic acid oil. Briefly, 36mL of 40% Sodium hydroxide solution was added to 100g oleic acid(approx 1:1 mole ratio) and stirred until the solution formed wax like clumps. The sodium oleate was then allowed to dry until it formed white tallow like clumps. Finally high quality sodium oleate(TCI 95%) was purchased.

The actual nanoparticle synthesis was done by dissolving approximately 10g of the previously mentioned iron oleate complexes in 100g of 1-octadecene. The solution was then heated to boiling(approx. 315°C for octadecene) under reflux and a nitrogen stream. The solution was allowed to vigorously boil for 30 minutes.

After the nanoparticle nucleation, the solution was allowed to cool down. The nanoparticles were extracted by precipitating them out with approx 250mL of ethanol. The particles were subsequently washed three times with a 3:2 mixture of chloroform and methanol. The final product was then dried.

Co-precipitation

Co-precipitation was performed by using Iron(III) trichloride as the Ferric Iron source and either Iron(II) dichloride or Iron(II) Sulfate as the Ferrous Iron source, typically in a 2:1 Ferric to Ferrous molar ratio.

Classical Co-precipitation

Typically 10mL of 0.2 M iron(III) Trichloride, 10mL of 0.1 M Ferrous iron source and 75 mL of water were mixed together and degassed to remove oxygen from the solution. This solution was then moved to a round bottom flask connected to a mechanical stirrer and kept under Nitrogen. With vigorous stirring 5mL of 28% NH_3OH were added to the solution to activate the nanoparticle nucleation. To stop the ripening, 2g of Trisodium

citrate were added to the solution. Typically 10 minutes after base addition. The solution was then heated up to 70°C and kept at that temperature for 1 hour. After this the solution was allowed to cool down and the particles washed by precipitating them with ethanol and resuspending them in basic milli-Q water. To produce a fine powder, e.g. for XRD analysis or magnetometry, the precipitate was freeze dried. The nanoparticle concentration of the final dispersion was measured by drying out an aliquot of the dispersion on a plate and weighing the final dried product, figure 6.3.

Dropwise synthesis

In an attempt to achieve higher crystallinity a modified version of the above described protocol was also used, adapted from [27]. Using a reverse ratio of Ferric to Ferrous iron atoms (1:2) and with slow addition of dilute ammonium hydroxide solution. Typically 2.5mL of the above mentioned 0.2M Iron(III) trichloride solution was mixed with 10mL of the 0.1M Iron(II) Sulfate solution and diluted to 100mL with water. Under nitrogen and rigorous stirring 20mL of 2M ammonium hydroxide was added to the solution at the approximate rate of 3mL/minute. The solution was allowed to age for 10-40 minutes after the base addition was over. The surfactant addition and washing or drying were performed as described above.

2.2.2 Silica coating

Iron oxide nanoparticles were stabilized and prepared for further modification by coating the iron cores with silica to make a core shell particle. This was achieved using a modified Stöber process [50, 54].

Briefly, 25ml of water were mixed with 75mL of Ethanol and the pH adjusted by adding ammonium hydroxide to 10 for smaller particles and 11-12 for larger. Under stirring, approximately 20-30mg of Iron oxide nanoparticles in dispersion were added to this solution. The silication was achieved by adding TEOS in several steps with two hours in between each step: 100 μ L, 200 μ L 500 μ L, 500 μ L, 500 μ L and 500 μ L to 1mL of TEOS and then allowed to stir overnight. The particles were washed by centrifuging. The particles were either resuspended in water or the supernatant removed and the precipitate freeze dried to produce a fine powder.

2.2.3 Functionalization

Synthesis of fluorescent Silica coated particles

Several different strategies were evaluated for the conjugation of the fluorescent molecule Rhodamine B to silica coated nanoparticles. Rhodamine B was conjugated to APTES through EDAC/NHS chemistry, either by first conjugating APTES to the surface of the nanoparticles or by conjugating Rhodamine B to APTES and then conjugating the whole

molecule to the silica surface. A third strategy attempted to introduce the Rhodamine B-APTES molecule to the silica coating condensation to make a fluorescent doped shell.

1. APTES coating of surface with subsequent Rhodamine B conjugation

APTES coating of silica was done using a protocol adapted from [50]. Silica coated iron oxide nanoparticles were dispersed in 30mL of water at a concentration of 1 *mg/mL*. Under stirring 30mL of Ethanol were added to the dispersion and the pH adjusted to 11. To this mixture 10 μ L of APTES were added and allowed to stir for approx 5 hours. The mixture was then centrifuged and the resulting precipitate freeze dried.

Rhodamine B conjugation was done by dispersing the APTES coated particles in water adjusted to pH 5, since amide bond formation occurs with highest yield in the range of pH 4 to 6 for EDAC/NHS chemistry [55]. Typically 10mg of Rhodamine, 10mg of EDAC, 6mg of NHS were mixed in and the solution allowed to stir overnight. The particles were separated by centrifugation.

2. Rhodamine B conjugated to APTES and then the particles

This conjugation is adapted from a protocol in [35] Typically 10mg of Rhodamine, 10mg of EDAC, 6mg of NHS and 2.5 μ L of APTES(approx. 2:5:5:1 mole ratio) were mixed in 10mL of DMSO and allowed to stir for 3-4 hours. Meanwhile the powder of silica coated iron oxide cores was dispersed in toluene, around 20mg in 40mL(Usually at no higher of a concentration than 0.5mg/mL). The solutions were then mixed under stirring and allowed to mix for 20-24 hours until the particles were separated out by centrifuging.

The particles were washed twice with toluene and twice with ethanol and then redispersed in water.

3. Dye doping

Dye doping was done by conjugating Rhodamine B to APTES by EDAC/NHS chemistry in DMSO using the same ratios as described above. Typically 1-5 mL of this mixture were added to the silica coating mixture(section 2.2.2) and the coating procedure continued as usual.

Every conjugation method ended with the particles dialysed(Spectra/Por Dialysis membrane, MWCO:12-14,000) in water adjusted to pH 10 for 24-48 hours to remove excess Rhodamine B.

2.2.4 Characterization

Imaging

The size and shape of the as prepared and functionalized nanoparticles was determined using a scanning electron microscope(Zeiss 1540 XB) and a transmission electron

microscope(Jeol JEM-1010) with an acceleration voltage of 60kV. For the SEM the samples were prepared by drying an aliquot of the nanoparticle dispersion on a 1X1cm doped silica plate. For the TEM the samples were deposited on a carbon-coated glow discharged 400 mesh nickel grids. The as prepared iron oxide cores were imaged without staining but the silica coated cores were stained with one drop of 0.5% phosphotungstic acid before imaging.

Fluorescence imaging

The fluorescence spectra of Rhodamine B and Rhodamine B conjugated particles was measured using a Chronos DFD spectrophotometer(ISS, Model:90021).

Dynamic light scattering and zeta potential

The zeta potentials, hydrodynamic radius of particles in dispersion and their polydispersity was measured using a Malvern Zetasizer(Nano ZS series). All measurements were done with appropriate parameters adjusted for solvent and material. Measurements were considered of good quality only when they fit the criteria of the Zetasizer software.

X-ray diffraction

Powder X-ray diffraction(XRD) was measured with Cu-K α radiation(1.50598Å) ranging from $2\theta = 10^\circ$ to 80° with a step size of 0.00164 and scan speed of 0.0003 using a Malvern-Panalytical Empyrean diffractometer. The average crystallite size was determined from the full width half maximum(FWHM) of the (311) diffraction peak of magnetite using Scherrer's formula. The top is typically visible at $2\theta \approx 35.5^\circ$, see figure 6.1. Gaussian peak fitting and FWHM calculation was done in Origin software(2019b).

Magnetometry

The magnetic properties of the particles produced in this project were analyzed using a vibrating sample magnetometer(Quantum Design, P525 PPMS) in fields up to 3 Tesla. The field dependant magnetization of the samples was measured by sweeping the applied field until sample saturation.

Results 3

This section presents the results of magnetic nanoparticle synthesis, their coating with silica and the conjugation of a fluorescent probe.

3.1 Synthesis of magnetic iron cores

Magnetic nanoparticles were synthesized using co-precipitation and thermal decomposition. Key parameters of these particles such as size, crystallinity and magnetic properties were analyzed.

3.1.1 Co-precipitation

The first synthesis of iron-oxide nanoparticles (IONPs) was done with the method of co-precipitation. This synthesis produced a dark black dispersion of particles that responded weakly to a magnet but not strongly enough for them to be separated out by it. So, the dispersion was frozen and subsequently freeze dried giving a fine black powder. This powder was clearly magnetic and could be manipulated with a magnet. A portion of this powder was resuspended in slightly basic water (pH 9) and a sample from it was prepared for the scanning electron microscope (SEM), figure 3.1.

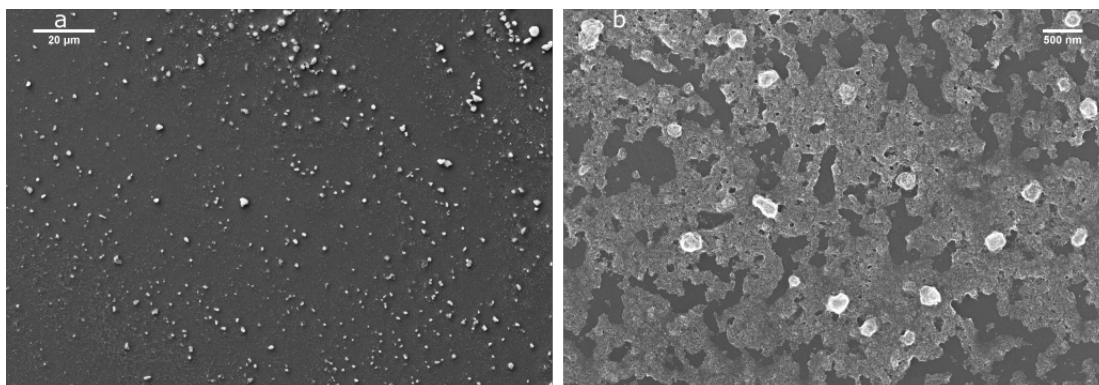


Figure 3.1: SEM imaging of IONPs from the first synthesis. a) Large aggregates. b) Smaller aggregates and visible salt/leftover reagents from the synthesis.

When imaged in the SEM the particles showed major aggregation forming multiple clusters in the range of microns, figure 3.1 a). There were some smaller particles in the range of a few hundred nanometers but the expected size from a successful co-precipitation is in the range of tens of nanometers. There was also the problem of the visible salt and left-over reagent which could interfere with further experiments, figure b).

In later synthesis the particles were not dried out but the colloidal solution measured in dynamic light scattering(DLS) immediately after synthesis. Typically the DLS measurements showed the diameter of the as-prepared particles to be around 40nm with some minor clusters visible, figure 3.2. The particles from these syntheses were washed by precipitating them out by adding ethanol and collecting them using a strong magnet. The supernatant was removed and the particles resuspended as before in basic water. DLS measurements showed that there was no increase in the diameter of particles washed this way.

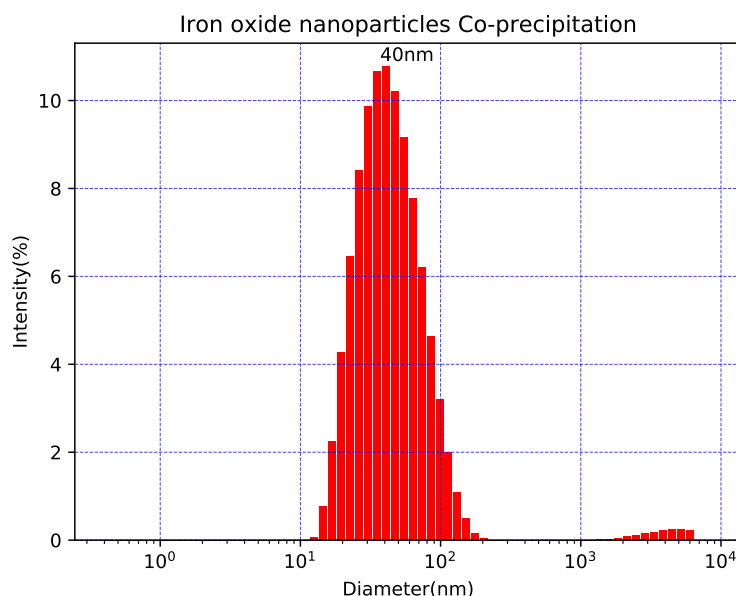


Figure 3.2: DLS histogram of IONPs synthesized using co-precipitation

When this sample was imaged in the SEM it did not show clustering to the same extent as the previous sample but none the less the sample had clearly aggregated when dried out for imaging 3.3. In figure b) there is a large aggregate of what seem to be multiple smaller particles, some of these aggregates are most likely due to the attraction of the magnetic particles in the drying of the sample. The washing by ethanol precipitation also seemed to have done it's job with little if any of left over reagents or salts being visible.

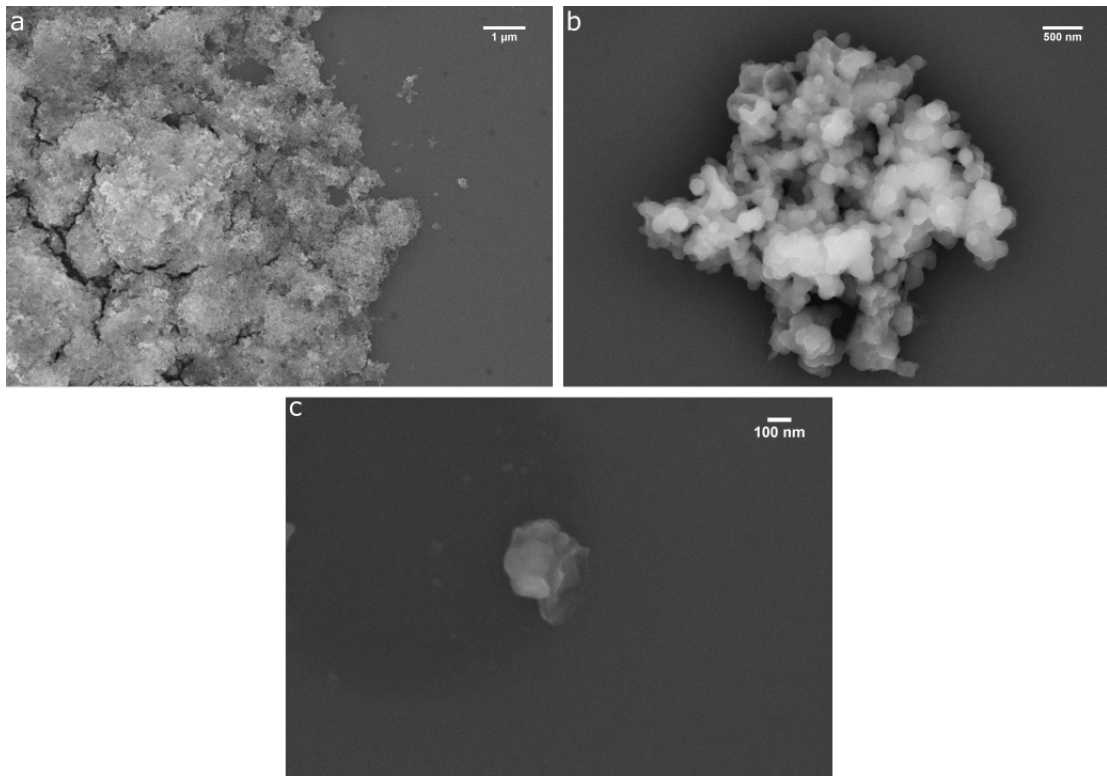


Figure 3.3: SEM imaging of IONPs from the second synthesis. a) A bed of aggregated IONPs, b) Multiple small IONPs aggregated, c) a large IONP, possibly with several smaller IONPs around it

The crystallinity of the particles was examined by powder XRD analysis. The crystallite size of particles prepared with sulfate and dichloride as the ferrous iron source in the synthesis was compared. The nanoparticle powder showed poor crystallinity with broad, barely visible peaks 3.4. The calculated crystallite size of particles from the dichloride synthesis was only 7.9nm and the sulfate synthesis 8.7nm. Although the peaks were broad they did fit the 2θ position that would be expected of magnetite.

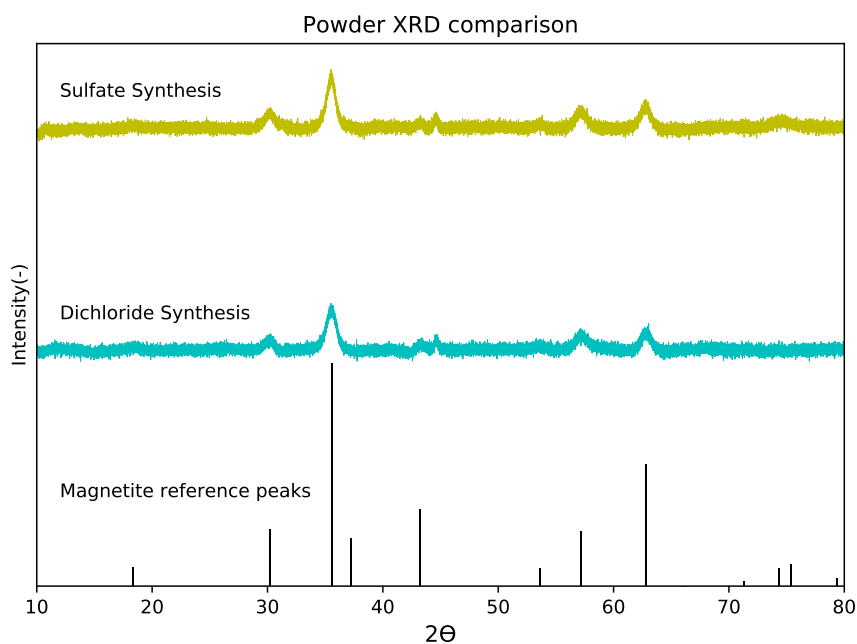


Figure 3.4: The XRD powder diffractograms of particles prepared from sulfate and dichloride synthesis with reference peaks for magnetite.

The measured crystallite size of the nanoparticles was much smaller than the core size according to DLS. To get a clearer image of the particles they were imaged using in a TEM, figure 3.5. The TEM revealed that the actual particle diameter was closer to 10nm for the sulfate synthesis a) (by manual measurement), and for the particles from the dichloride synthesis was 6.8, figure b). The diameter of the particles measured in the TEM is considerably smaller than the one measured by DLS. This indicates that the particles exist as clusters of multiple smaller particles when in dispersion.

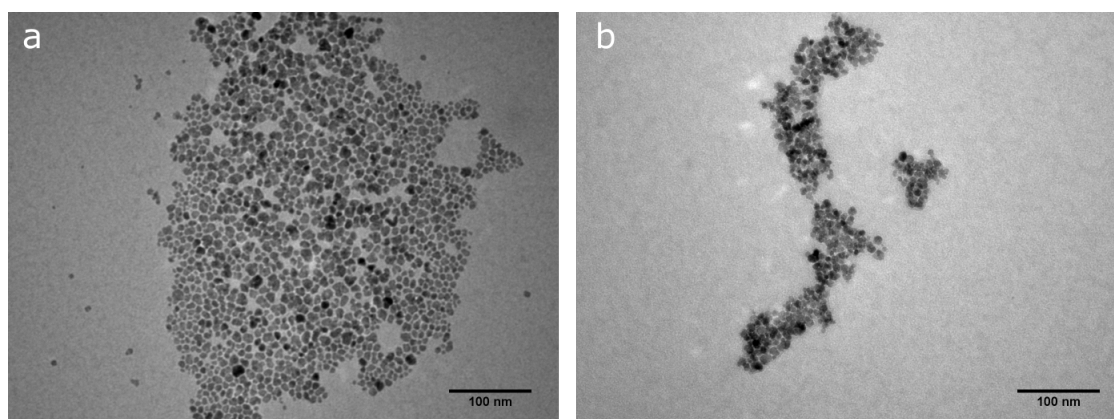


Figure 3.5: TEM images of IONPs from a) Sulfate synthesis and b) Dichloride synthesis.

In an attempt to increase the crystallinity and size of the particles the synthesis was repeated using a modified version of the co-precipitation protocol, referred to from now on as "Dropwise synthesis". This synthesis was itself also repeated with a longer nucleation time to see what effect that would have on the particle size and crystallinity.

The size of particles from the dropwise synthesis was measured by DLS. It was similar to the ones for the classical coprecipitation but giving the solution a longer nucleation time gave a larger average diameter, left figure 3.6 This dispersion was filtered giving a monodisperse size distribution of smaller cores, right figure 3.6.

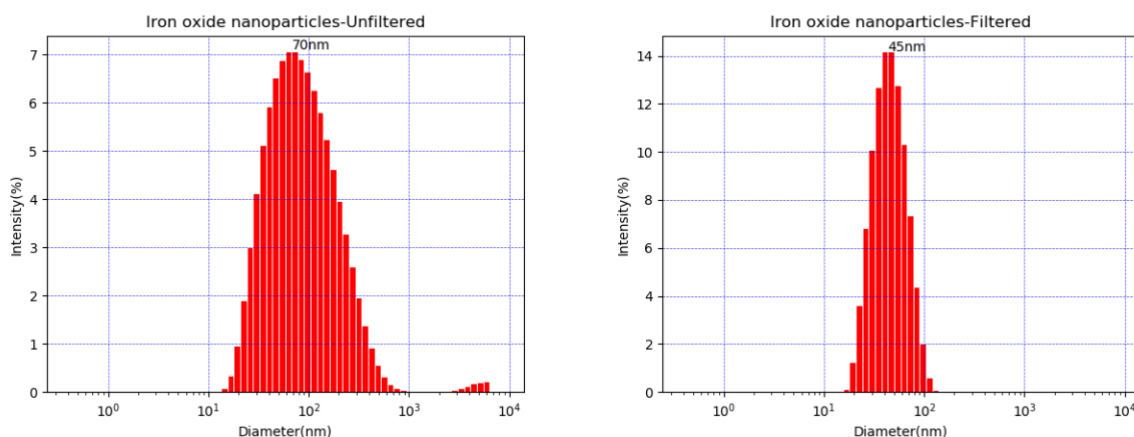


Figure 3.6: DLS histograms of the Dropwise synthesis with an extended nucleation time. Left: Unfiltered dispersion, Right: Filtered dispersion

The size of the particles from the dropwise synthesis was measured by TEM, figure 3.7. As before, the actual size of individual particles was smaller than the measured hydrodynamic diameter in DLS. However the particles from the dropwise synthesis were larger than from the classical co-precipitation, on average 16.9nm for the dropwise and 21.4 for the long nucleation synthesis.

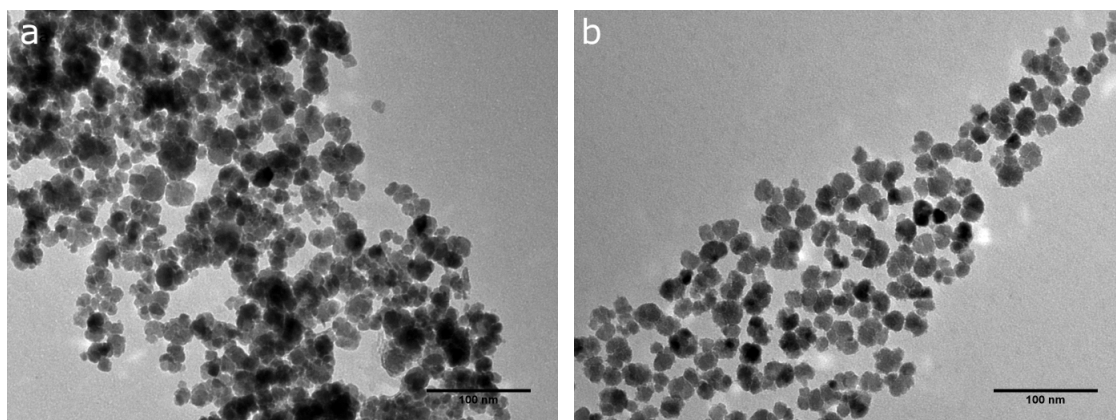


Figure 3.7: TEM images of IONPs from the dropwise synthesis. a) Normal nucleation time, b) Longer nucleation+Filtering.

The particles from the dropwise synthesis were also analyzed by XRD powder diffraction 3.8. The crystallite size showed a minor improvement over classical co-precipitation but was also considerably lower than the diameter of the particles. Dropwise synthesis had a crystallite size of 12.6nm while the longer synthesis was 14.3nm. To test whether or not oxidation of magnetite was causing the low crystallinity a dropwise synthesis without an inert atmosphere was done. The crystallite size of this synthesis was 12.3nm, very similar to that of the previous dropwise synthesis.

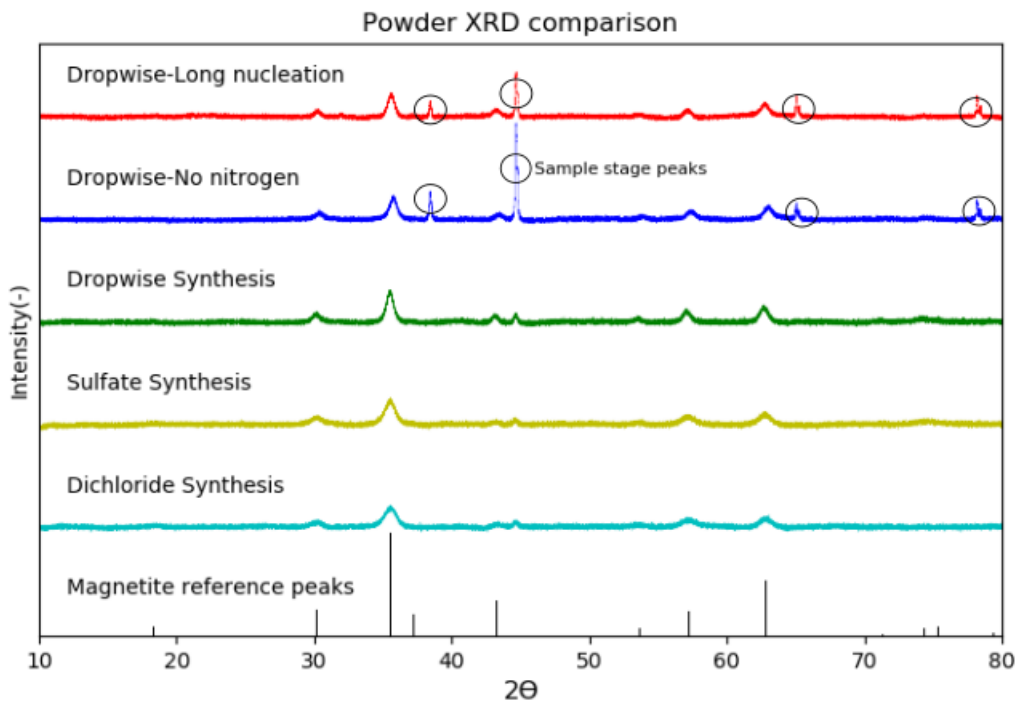


Figure 3.8: XRD diffractogram of all IONP synthesis methods. The sample stage peaks can be seen in some samples, see figure 6.2

The magnetic properties of the nanoparticle powders were measured using a vibrating sample magnetometer(VSM), figure 3.9. All of the syntheses showed clear superparamagnetic(SPM) behaviour with no clear hysteresis loops. The saturation magnetisation(M_S) seems to grow with increasing crystallite size except for the dropwise synthesis with longer nucleation time which showed the lowest saturation magnetisation of all the samples.

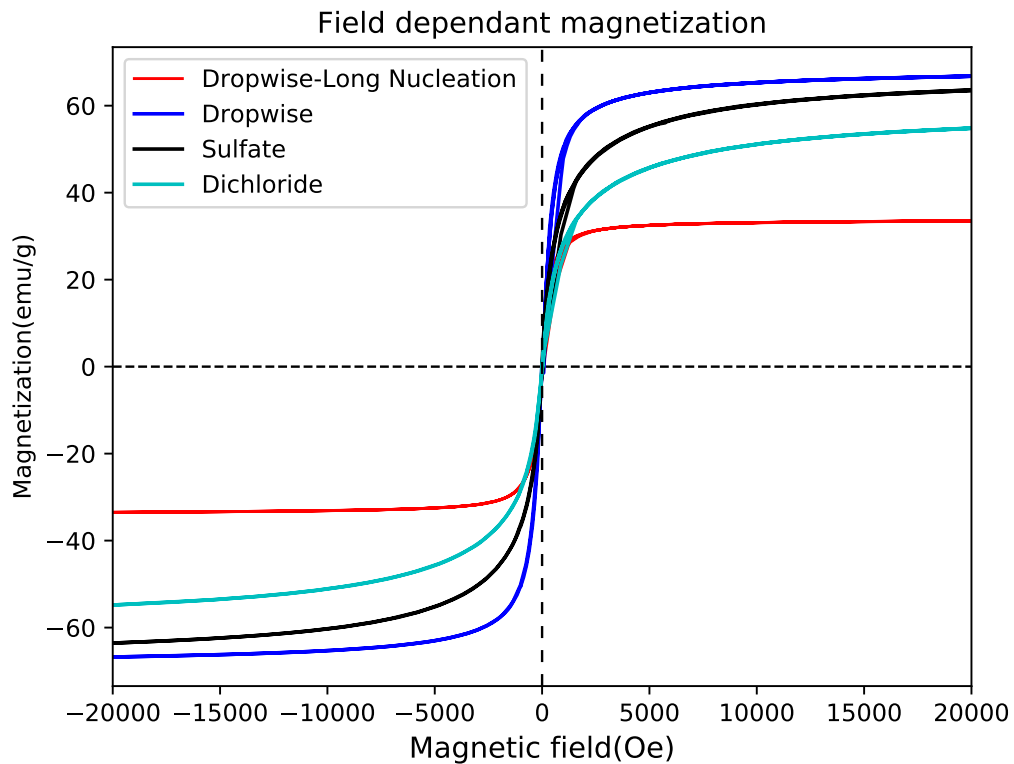


Figure 3.9: Magnetization curves of superparamagnetic IONPs.

3.1.2 Thermal decomposition

IONPs were also synthesized by thermal decomposition. This method of synthesis requires organometallic precursors such as iron oleate which was itself first synthesized. Several strategies were evaluated for the synthesis of iron oleate.

Firstly the iron-oleate was synthesized using oleic acid oil as the source of the fatty acid for the complex. This method of synthesis gave a black oily liquid but not a wax which would be expected of iron oleate. When the reaction mixture was washed the water was yellow, indicating unreacted iron(III) in solution. Thermal decomposition using this liquid gave no detectable nanoparticles.

Secondly, sodium oleate was synthesized by saponification of the previously mentioned oleic acid. Iron oleate synthesis using this source of the fatty acid gave a reddish wax like substance. The aqueous phase was clear and did not appear to contain left-over iron(III). Thermal decomposition of this substance gave a black oily liquid. This fluid did not respond to a magnet nor could any particles be isolated from it.

Finally sodium oleate was used to make iron oleate. This method gave a similar reddish wax as before, however it was darker and less fluid. Thermal decomposition of this substance gave a dark black liquid which could be manipulated with a magnet. Magnetic nanoparticles could be isolated but even with multiple washes the dried product did not give a fine powder but rather a thick black liquid.

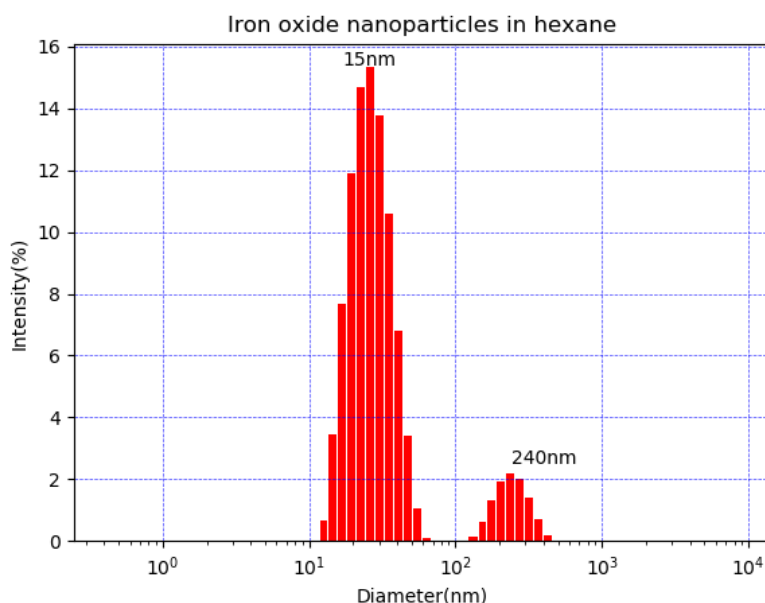


Figure 3.10: DLS histogram of IONPs synthesized by thermal decomposition.

These size and distribution of these particles was evaluated by DLS, figure 3.10. The size was monodisperse, primarily centered around 15nm in diameter with some minor clusters, about 240nm in diameter

TEM imaging showed the particles to be highly monodisperse with the average sizes of individual particles very close to the 15nm measured by DLS with a manually measured average diameter of 16.2nm, figure 3.11(Left). There was however many tiny particles which were not detected in DLS. These tiny particles were measured to be 3-5nm in diameter(right figure).

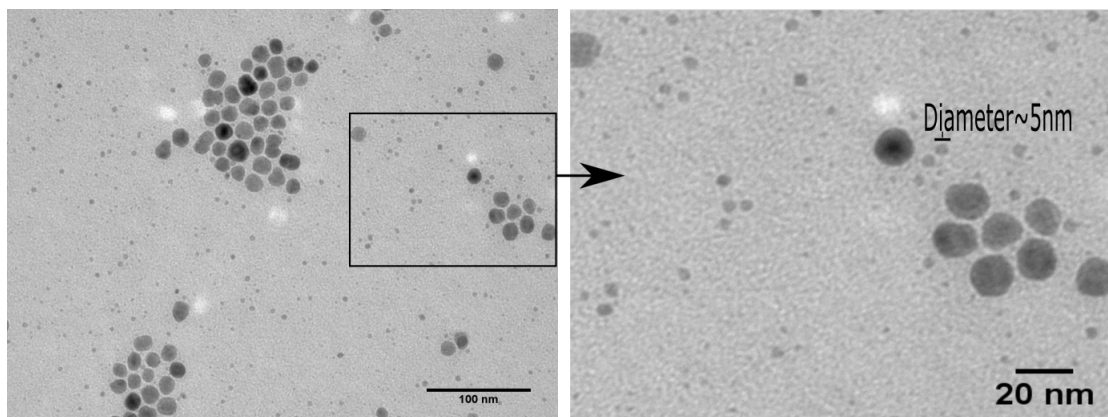


Figure 3.11: TEM images of IONPs synthesized by thermal decomposition.

3.1.3 Summary of IONP synthesis

A summary of the size, crystallinity and magnetic properties of the synthesized IONPs are presented in table 3.1.3.

Table 3.1: A summary of the results for the synthesis of IONPs.

Synthesis	Diameter(nm): TEM	Diameter(nm): DLS	Crystallite size (nm)	Saturation magnetization (emu/g).
Dichloride	6.8	32	7.9	54.9
Sulfate	10.0	40	8.7	63.6
Dropwise	16.9	na	12.6	66.9
Dropwise	21.4	45	14.3	33.5
Long nucleation				
Thermal	16.2	15nm	na	na
Decomposition				

3.2 Silica coating

Iron oxide cores synthesized with co-precipitation were coated with silica using a modified stöber process. The coated particles showed decent stability in water and had a measured zeta potential of -47.5mV at pH 11. SEM imaging of the coated particles showed monodisperse spherical particles, figure 3.12 a). The particles can be see forming unusual aggregates, figure b). This is most likely caused by the magnetic cores attracting each other during the drying out of the sample.

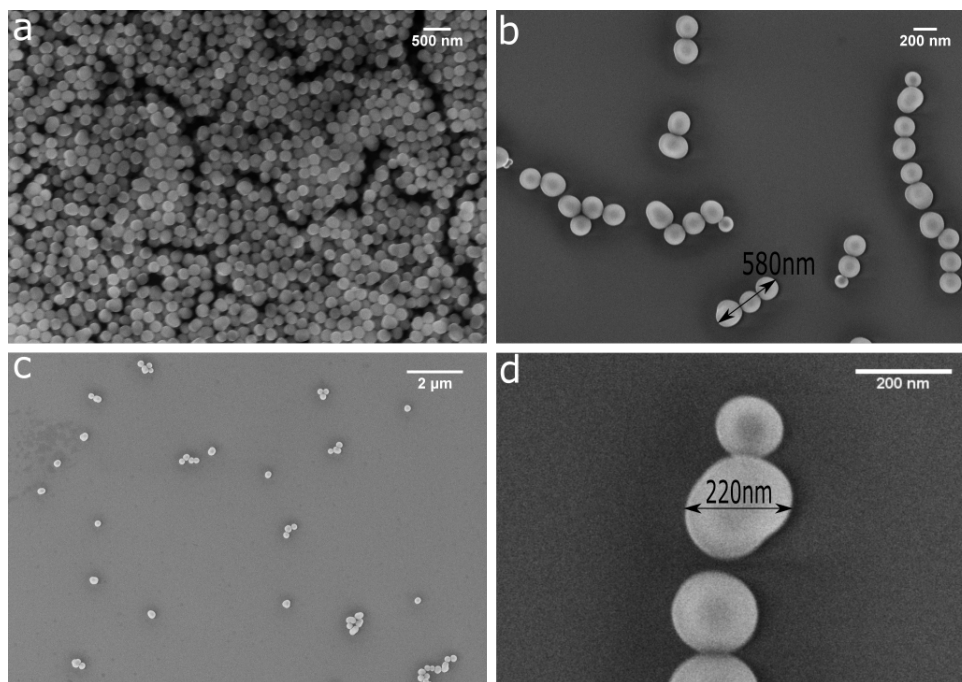


Figure 3.12: SEM imaging of silica coated iron cores. a) A large amount of spherical core shell particles, b) particles forming magnetic assemblies, c) Small aggregates of particles, d) Zoom in of figure b)

The average diameter of dispersed particles measured by DLS was 270nm , figure 3.13, but a manual count of the particles in figure a) showed the average diameter to be 190nm . Most likely the particles exist in dispersion as aggregates of a few particles as can be seen in figure 3.12 c). The DLS did not show any major clustering on the order of micrometers as was typically seen in the iron cores.

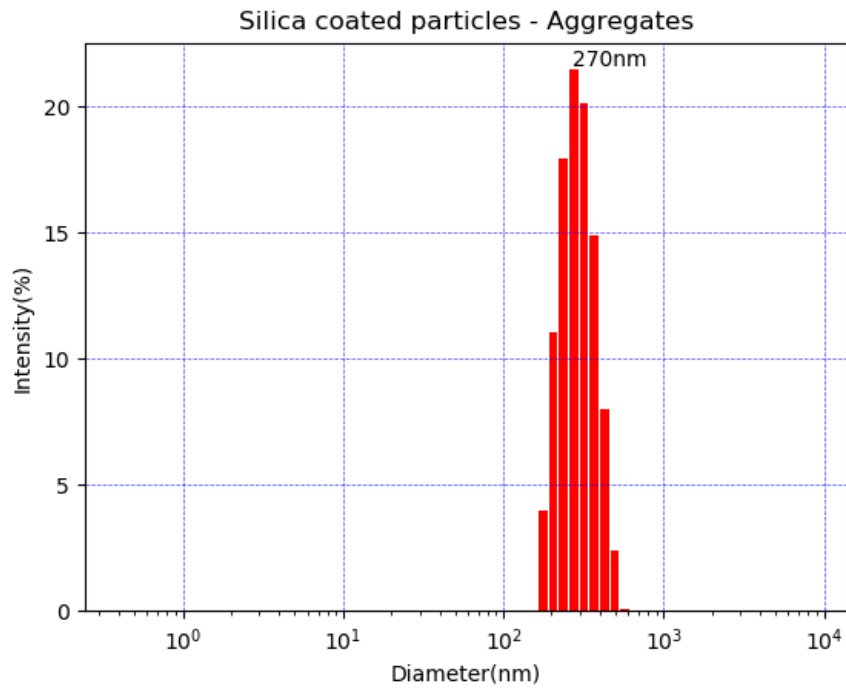


Figure 3.13: DLS histogram of silica coated nanoparticles

TEM imaging of these particles shows them to be the same size and shape as the in the SEM. However the TEM does reveal the rough and amorphous surface which would be expected of a silica coating. It was however not possible to see the encapsulated iron cores, figure 3.14.

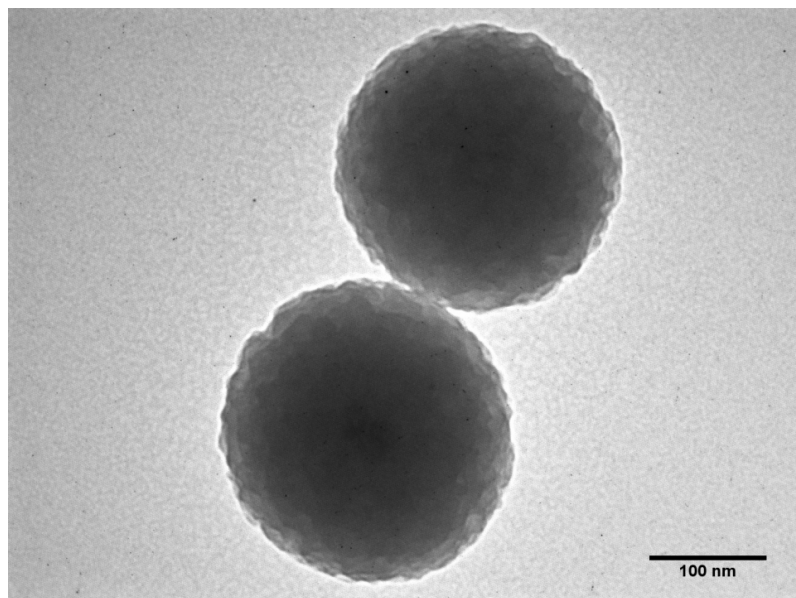


Figure 3.14: TEM imaging of silica coated nanoparticles

The silica coating was repeated to make smaller shells on the particles. These particles were also imaged using the TEM, figure 3.15. The particles were considerably smaller in size and the iron cores could clearly be seen encapsulated within the silica shell

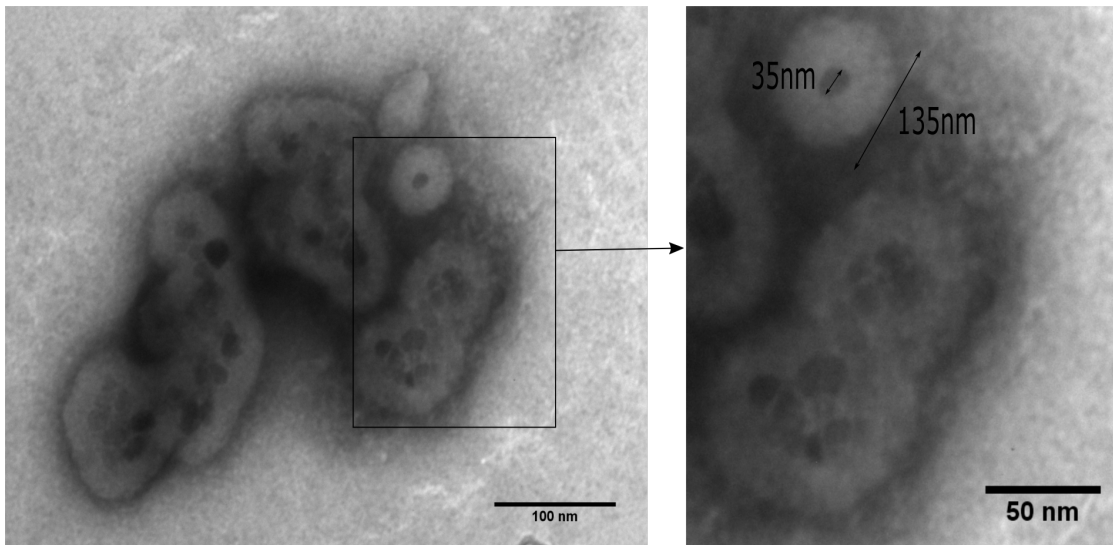


Figure 3.15: TEM images of silica coated iron oxide cores

The particles however are for the most part not clearly spherical and show major aggregation. The larger iron cores used, from the dropwise synthesis seem to aggregate before the coating can cover individual cores. The cores can be seen forming long assemblies of multiple cores which the silica then coats, figure 3.16.

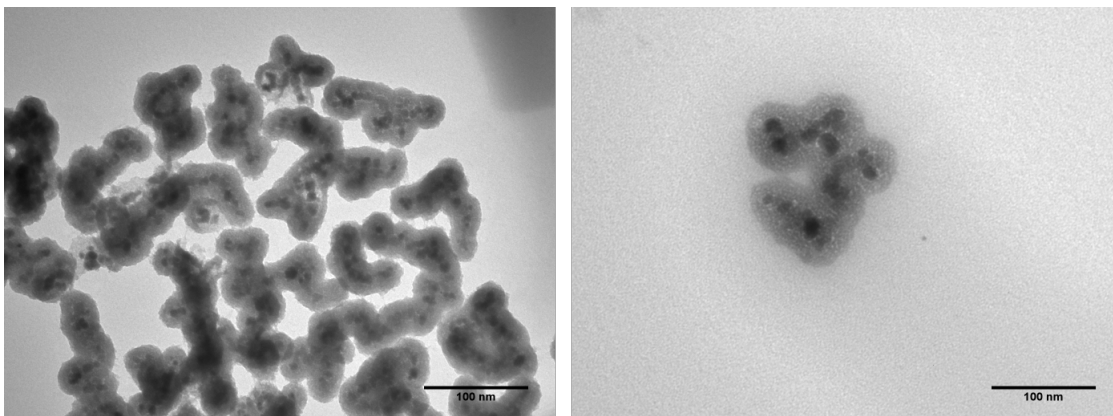


Figure 3.16: TEM images of silica coated iron oxide cores

The magnetization curve of the silica coated iron clusters seen in figure 3.16 was measured by VSM. The saturation magnetization of the silica coated particles was approximately $\frac{1}{6}$ th of the naked IONPs, figure 3.17.

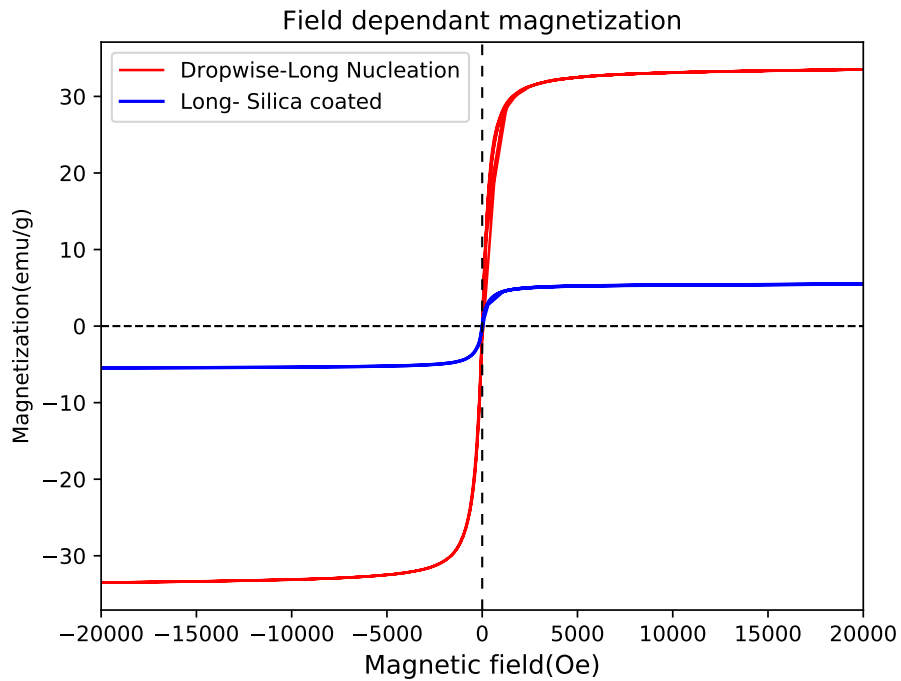


Figure 3.17: Comparison of the magnetization curves of coated and uncoated IONPs

3.3 Rhodamine B conjugation

Rhodamine B was conjugated to the surface of the nanoparticles through EDAC/NHS conjugation chemistry and the linker molecule APTES. Several different strategies were evaluated for the conjugation.

Conjugation in ethanol/water

Conjugation of APTES to the surface of silica coated particles was confirmed by measuring the zeta potential of the coated particles at pH 6 and 10. At pH 6 silica particles have a negative zeta potential but the APTES coated particles had a zeta potential of +14mV. At pH 10 the particles had a negative zeta potential of -38mV. Rhodamine B conjugation to the amine group of APTES seemed to be successful since the particles showed strong fluorescence even after dialysis to remove excess dye.

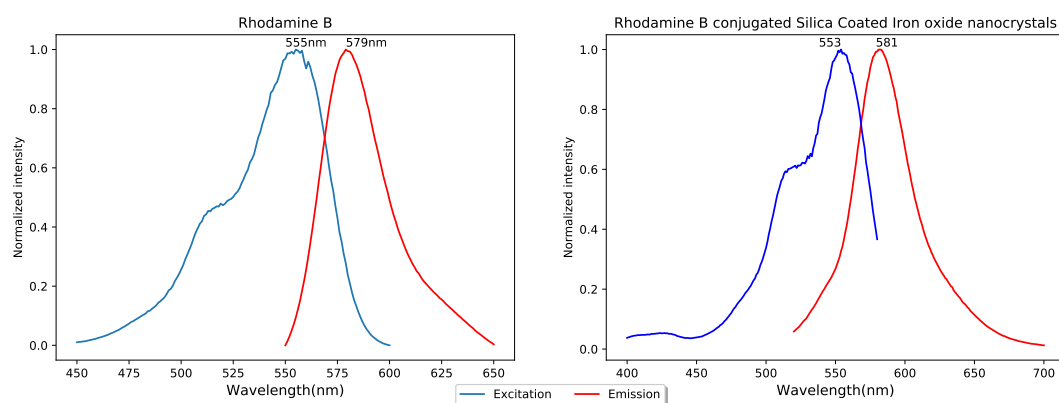


Figure 3.18: Normalized fluorescence spectra of Rhodamine B(Left) and Rhodamine B conjugated silica coated particles(Right). Wavelengths of highest excitation and emission are marked on the graphs.

The particles showed major aggregation when imaged in the SEM. A large amount of debris was visible that could not be contributed to the silica particles, figure 3.19 . Most likely this is the cause of APTES molecules crosslinking and forming aggregates. Although the dispersion was measured to be fluorescent it is possible that it stems from Rhodamine B conjugated to aggregates of APTES rather than the APTES coating the surface of the silica particles.

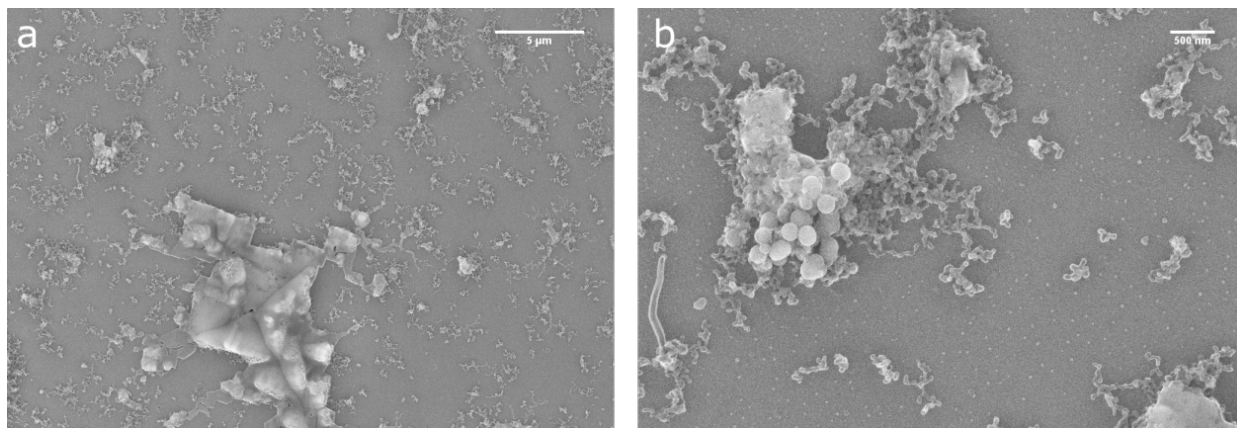


Figure 3.19: SEM imaging of Rhodamine B conjugated Silica coated particles. a) Large aggregates. b) Particle and APTES aggregates

Dye doping

Dye doping of silica coated particles gave a dispersion of large aggregates with an average diameter of over a micrometer (Finna DLS histogram). The particles showed no detectable fluorescence. SEM imaging showed large aggregates of particles, figure 3.20 a). Figure b) shows much smaller particles which could possibly just be APTES aggregates fused with each other as well as particles.

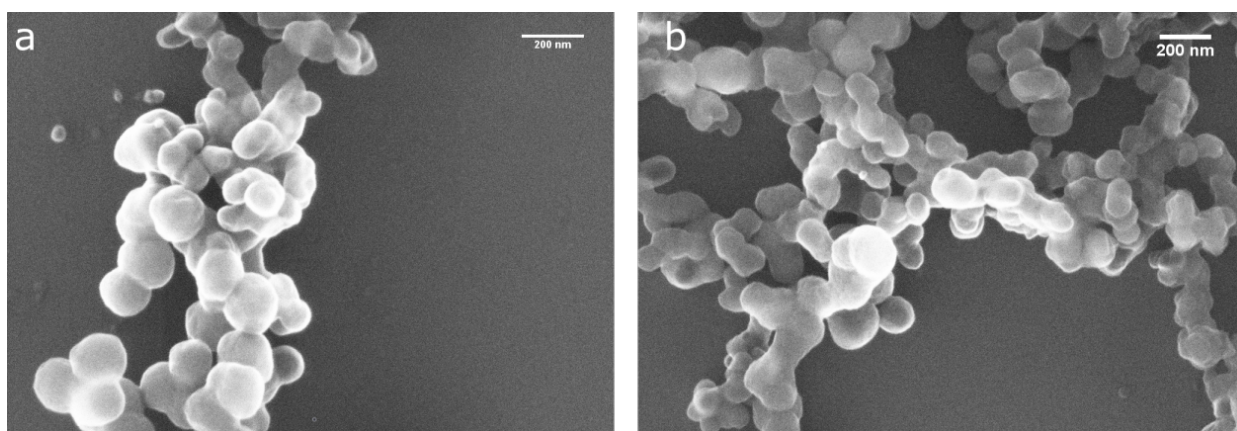


Figure 3.20: SEM images of Dye doped silica particles. a) Particle aggregates, b) Possibly APTES aggregates

Conjugation in Toluene

Due to the aggregation phenomena seen aqueous dispersions the fluorescent dye conjugation was performed in the organic solvent toluene. The particles showed fluorescence similar to that of Rhodamine B but with a excitation peak that had shifted downwards from 555nm to 538nm, figure 3.21.

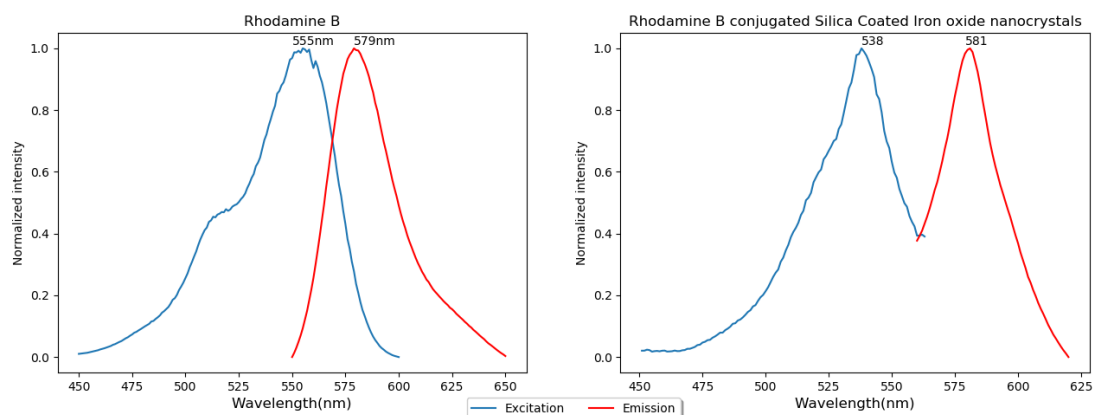


Figure 3.21: Normalized fluorescence spectra of Rhodamine B(Left) and Rhodamine B conjugated silica coated particles(Right) from the Tolene coating procedure. Wavelengths of highest excitation and emission are marked on the graphs.

When imaged in the SEM there were large aggregates visible in the sample, figure 3.22 a). When zoomed in there were clearly multiple smaller particles visible, figure b). These particles are most likely more of the APTES aggregates.

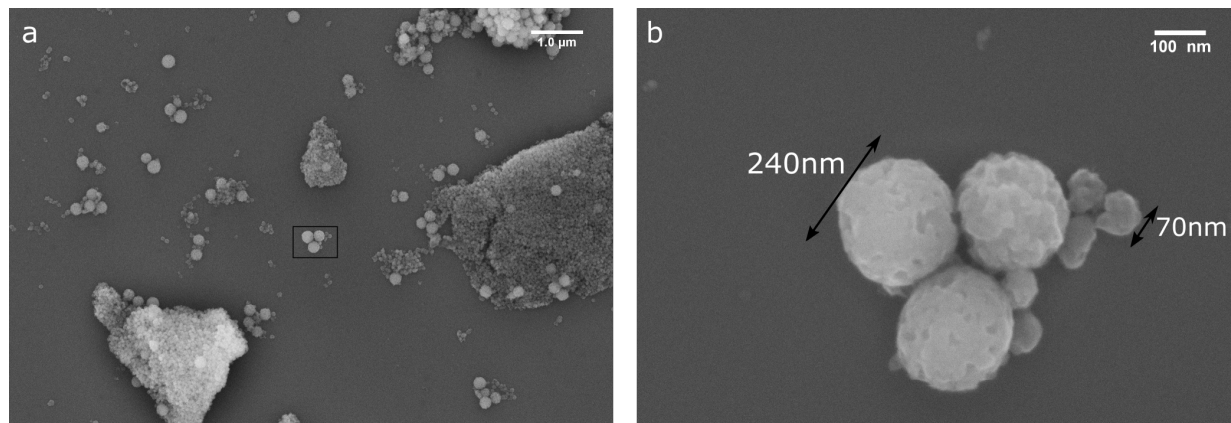


Figure 3.22: SEM imaging of silica coated IONPs conjugated to Rhodamine B in toluene

Discussion 4

As was mentioned in the introduction there has been a healthy amount of interest in the use of magnetic nanoparticle in biomedicine and there exists a multitude of articles with different ways to achieve this. However, the articles focusing on producing multifunctional magnetic drug carriers most often follow a similar scheme. Typically it starts with the synthesis of the magnetic core followed by the coating of it with a protective shell and the addition of fluorescent and drug carrying abilities. Finally the nanocarriers are sterically stabilized by polymers. There of course exist different variations of these strategies but the scheme is effectively the same in multiple articles. [35, 47–50]. In this project it was attempted to follow this scheme to produce a multifunctional magnetic particle. This section discusses the results of magnetic core synthesis, then the coating of cores with silica and finally the conjugation of a fluorescent probe.

4.1 Iron core synthesis

Magnetic nanoparticles are the foundation of any magnetic drug delivery system. For this project they were synthesized using two different methods and with multiple variations of these methods. The most important parameters of these particles are their size, dispersity and their magnetic properties. For drug delivery purposes it is desirable to have the strongest possible magnetic response while remaining on the nanoscale with regards to size.

4.1.1 Co-precipitation

Early attempts at synthesis from this protocol showed major aggregation of particles and did not produce a stable colloidal dispersion. However by refining the protocol and not drying out the particles at any stage, they formed a stable dispersion. It is clear that the particles aggregated through the drying out process, however the particles most likely also aggregate when precipitated out with ethanol. The ethanol aggregation is however easily reversible when the particles are redispersed without ever drying them. The citrate coating seems to be an effective surfactant through this process since no increase in the average diameter is seen after ethanol precipitation.

The citrate coated particles showed decent stability between pH 8-9, staying for the most part stably dispersed for months in dispersion, see figure 3.2. Although there was the

problem of some major clusters in the micrometer range forming after extended periods. The electrostatic repulsion stemming from citrate is pH dependant and is based on the disassociation of the carboxylic groups, which should be fully disassociated at basic pH [56]. Furthermore magnetite can dissolve in acidic medium making it highly undesirable to keep particles at lower pH [26].

The diameter of particles synthesized by co-precipitation, measured by DLS was in the range of what is desired for the magnetic core of a core shell particle, perhaps on the larger side. Although a diameter of around 40nm does give ample room for further modification such as silica coating or polymer conjugation while still remaining in the narrow window of size restrictions for nanocarriers that can function in the blood, see section 1.2.3.

The crystallinity of these particles at first appeared quite poor, with the crystallite size being less than a third of the diameter measured in DLS. The crystallinity is an important parameter since it directly correlates with magnetic properties [57]. So this was a cause of concern.

However the actual particle size measured by TEM showed the individual cores to be only around 10nm on average for e.g. dichloride and sulfate synthesis. The as synthesized dispersion of particles is therefore actually a dispersion of particle clusters. This is not necessarily a problem, e.g. Wan et. al. deliberately clustered IONPs for a larger effective core which retained superparamagnetic properties [48]. As long as the particles exhibit strong enough magnetic properties for the task at hand it makes little difference whether or not the cores are clusters or single particles.

Most likely the clusters form immediately during synthesis. The citrate coating does increase the zeta potential of the IONPs, but it does not offer much in the way of steric stabilization. These clusters have higher porosity and therefore have weaker VdW attraction, which favors colloidal stability making them the more stable than individual particles [58].

There is some evidence that the formation and crystal growth of magnetite nanoparticles is influenced by the anionic species existing with ferric ions in the solution. Ions can both inhibit and aid in the crystal growth through influencing the zeta potential of particles. Iwasaki et al. described the use of reverse ratios of ferrous and ferric iron salts compared to classical co-precipitation, to give larger crystallites with the theory that sulfate ions aided in the crystallization [27]. This synthesis referred to here as the dropwise synthesis, gave a larger crystallite size than either the dichloride or the sulfate synthesis, table 3.1.3.

Re-examining the crystallite size with the knowledge of the actual particles size from the TEM allows us to say that the particles are nearly single crystals. For example the crystallite size for sulfate synthesis was calculated to be 8.7nm while the diameter measured from the TEM images showed the average particle diameter to be 10.0nm. It is important

to note the fact that the product of magnetite oxidation, the ferrimagnetic maghemite is indistinguishable from magnetite by X-ray diffraction. To distinguish the two oxides it would take other methods like Mössbauer spectroscopy [59]. The presence of maghemite is not necessarily a major problem since it does not have a saturation magnetization close to 80% of that of magnetite [25].

The magnetic properties of the particles were similar to those seen in literature. For example the M_S of the particles from the dichloride and sulfate synthesis were 54.9 and 63.6(emu/g) respectively, but the bulk M_S of magnetite is considerably higher at 86(emu/g) [32]. The decrease in M_S with diameter is a known phenomena, Li et al. reported the M_S for particles with a diameter of 9.8nm to be 54.7(emu/g) and showed the M_S to increase to near bulk levels with greater diameters [57]. Since there is a critical diameter to superparamagnetism, there is a limit to how large the particles can become before losing their SPM properties. The theoretical critical diameter for spherical magnetite nanoparticles is approx. 17nm [45]. All but one sample prepared had an average diameter below 17nm but all the samples showed clear SPM behaviour with no detectable hysteresis loop. The only sample that had a diameter above the theoretical SPM limit was the dropwise synthesis with a long nucleation time. This sample had the largest crystallite size but perplexingly had by far the worst saturation magnetization of all the samples. When the size measured by TEM is compared to the crystallite size it can be seen that the TEM size is considerably larger than the crystallite size. Possibly there is a large magnetically dead layer on the surface of the particles which does not contribute to the magnetization of the sample.

The greatest M_S was seen in particles synthesized by dropwise synthesis, reaching about 78% of bulk M_S . This is highly similar to what would be expected of a maghemite nanoparticle, however it is impossible to say with the data available whether or not the particles are magnetite or maghemite or mixed phases of both. It is important to note though that it would be expected of maghemite powder to be brown, while all the samples did have a dark black colour [60].

4.1.2 Thermal decomposition

Thermal decomposition proved to be much more difficult than co-precipitation, requiring multiple attempts and some improvements in the experimental set-up until a successful synthesis was achieved. Partially these difficulties were caused by the problems with making the organometallic precursor, iron-oleate. The synthesis of this precursor was attempted with oleic acid and in-house synthesized sodium oleate but both of these syntheses failed to produce any detectable magnetic particles. The oleic acid used was only 66-88% pure. This made measuring out the oleic acid needed to react with the iron trichloride(3:1 ratio) difficult and possibly an excess amount was used. Excess oleic acid in the reaction can be problematic since it can actually delay nucleation by several hours

[31]. Possibly this is the reason for no particles being detected since it may have taken several hours more for particle nucleation than the synthesis was allowed to run.

Eventually a cheap source for the sodium oleate was found and the synthesis worked as intended. However it proved difficult to get the particles to form a fine powder, even after multiple washes both with ethanol and with a mixture of chloroform and methanol. It is possible that there is excess oleic acid and even octadecene that are present in the sample after all the washes. The sample could none the less be dispersed in hexane for further analysis.

In the TEM the particles showed good monodispersity and shape with a measured average diameter of very close to that of the one measured in DLS. The particles do not form large aggregates when dried out that make them difficult to measure like the ones from co-precipitation. This is likely thanks to the oleic acid which is a much larger surfactant compared to citrate. The TEM did reveal that there were multiple smaller particles that had not been seen in DLS. There are many of these particles and they seem to be 5nm or smaller in diameter. Most likely these particles could be made larger by having a longer nucleation time during the synthesis.

Due to major difficulties with both the synthesis and forming a powder the magnetic and crystal properties could not be investigated in the time frame of this project. There are articles that report IONPs with M_S close to bulk material, although they were synthesized with more complicated versions of thermal decomposition such as Unni et al. that reported IONPs with M_S of 74(emu/g) with a diameter of 21nm or Kemp et al. which synthesized particles with M_S of 80(emu/g) at a diameter of 20nm, both by controlled addition of oxygen to the reaction [32, 61].

Thermal decompositions seems to be the ideal IONP synthesis method when it comes to control of size, polydispersity and magnetic properties. However it proved to be considerably more complex than co precipitation as well as requiring the use of organic solvents. Particles that have oleic acid as a surfactant also seem to be more stable. There is almost no difference between the diameter measured in DLS and the one measured in TEM. There were also no clusters on the micrometer scale as are typically visible in co-precipitation. The oleic acid does however make the particles non dispersible in water, which is a requirement for most biomedical purposes. There are several strategies to make the particles water soluble such as silica coating the particles in a microemulsion system as done by Baddrudoza, [35] or by an aqueous phase transfer, see [62]

4.2 Silica coating

Silica coating of IONPs proved to have a stabilizing effect on them. As previously mentioned the IONPs proved difficult to fully resuspend when dried out without them forming major aggregates. The silica particles on the other hand readily suspended for the most part, albeit with ultrasound treatment. Although the silica coated particles did not form the inseparable clusters on the micrometer scale as were seen in dried out IONPs they still formed small clusters of several particles that were difficult to separate by ultrasound baths.

The particles proved to be monodisperse and showed interesting aggregation phenomena when imaged in the SEM which could be taken as evidence of them having encapsulated magnetic cores. However when imaged using the TEM no IONP cores could be seen. Most likely this is because the acceleration voltage of the TEM was too low for the thick shell of silica. For example Baddrudoza et al. and Wan et al. used acceleration voltages of 200kV for imaging of cores with considerably thinner shells of silica [35, 48] but the acceleration voltages used for the imaging of the particles in this project was 60kV. However with the synthesis of larger cores by the dropwise synthesis and a thinner coating protocol the cores could be proven to be encapsulated within the silica by TEM. However with this new coating protocol it seems as though the cores formed major aggregates before the coating could properly stabilize them. It is clear from the initial washing step that the IONPs aggregate to a great extent in ethanol or ethanol/water mixtures.

The coating mixture is approximately 75% ethanol and it is easy to imagine that these larger cores aggregate during the slow coating done at pH 10, before they can be properly stabilized by the silica shell. It should be possible to do the coating in a mixture with a higher water content. For example Chekina et al. performed the coating in approximately thirty percent ethanol [50]. The use of ultrasound during coating has also been reported. This seemingly helps with the dispersion of IONPs, preventing their aggregation. Another problem that the Stöber process is known to have is the formation of homogeneous silica particles due to the low critical concentration for nucleation [63]. Possibly some of the particles where no cores could be seen were only silica, not core shell particles.

The silica coated IONPs showed M_S that was considerably lower than that of the naked cores. This is a similar drop in M_S as can be seen in published articles [48]. This weaker magnetization is a trade off for the protective coating. It is also important to note that for intravenous magnetic drug targeting the fluidic force acting on the particle is a function of its size. This means that the increased size of particles by coating reduces their ability to be manipulated in vivo, see section 1.5.

4.3 Rhodamine B conjugation

There exists a great range of fluorescent dyes and even quantum dots that have been used to make multifunctional magnetic nanoparticles with imaging properties. However the iron oxide cores can quench the fluorophores when they are in direct contact with them. Because of this the particles are usually engineered in such a way that the fluorescent molecule is a safe distance away from the core [47].

Fluorescein, Rhodamine and their derivatives are some of the most popular fluorophores when it comes to bioconjugation and nanoparticle functionalization. More often than not their isothiocyanate derivatives are used due to their easy "click-chemistry" to amine groups such as the one present on the linker molecule APTES. An alternative to these expensive derivatives is to use the carboxyl group, present on both rhodamine B and fluorescein molecules for conjugation to amine groups through the EDAC/NHS coupling method. This has been reported with success for fluorescein but to the best of the authors knowledge it has not been reported before for rhodamine B [64].

The APTES linker molecule has been extensively used for conjugation chemistry with silica. The silane end of it can covalently bind to silica surface atoms while the amino group faces outwards, open for conjugation. Properly coated silica particles can be expected to have a positive zeta potential at biological pH. This has been used to make modified silica particles capable of binding DNA [65].

Unfortunately the APTES molecule can also cross link and form aggregates in a similar manner to the condensation of TEOS. This became apparent when the coupling chemistry was attempted in aqueous dispersion, figures 3.19 and 3.20. Possibly this aggregation could be avoided by using minuscule amounts of the linker molecule. However strong fluorescence is desirable so eventually the conjugation chemistry was attempted in organic solvents where aggregation should be less of a problem. The silica coated particles proved to be dispersible in toluene and a conjugation protocol for folic acid was adapted for the fluorescent dye binding [35]. However the APTES still aggregated in this coating protocol forming it's own particles, figure 3.22 b).

It is possible that the amount of reagents used for the coupling of fluorescent dye were too high for the amount of particle powder used. For example the amount of APTES used for the conjugation in toluene was approx $10\mu\text{L}$ which is proportionally more than was used in [35], where the protocol was adapted from. Future attempts of conjugation it could be attempted with smaller amounts of APTES for shorter mixing times.

Conclusion 5

The aim of this project was to synthesize magnetic nanoparticles and modify them for imaging and greater stability before testing them on a cell culture model. Magnetic iron oxide particle clusters were synthesized and shown to be in the size range necessary for intravenous use. The clusters had decent magnetic properties on par with published articles using the same methods. Different methods of synthesis were evaluated and compared, showing that using iron sulfate as the ferrous iron source for co-precipitation gave better crystallinity and magnetic properties than iron chloride. Particles synthesized using thermal decomposition gave excellent shape and dispersity but could not be fully characterized in the time frame of the project.

The nanoparticle clusters were coated with silica for stabilization and further functionalization. The coating proved successful in increasing the stability of the cores, making it possible to form powders which did not irreversibly aggregate such as had been seen in uncoated IONPs. Control over the thickness of the silica shell proved harder than expected with major aggregates of IONPs forming before the silica could properly coat them when a smaller shell protocol was used. The encapsulation of IONPs was however shown and the magnetic properties evaluated. Although there was a significant drop in the per gram saturation magnetization of coated cores it was no greater than what is reported in literature.

The conjugation of rhodamine B using a novel method proved to be problematic, not because of the coupling chemistry but rather the linker molecule APTES forming aggregates. The particle dispersion remained fluorescent after multiple washes and extended periods of dialysis to get rid of excess dye showing that most likely the dye was bound, either to the particles or the APTES aggregates. The results of the dye conjugation were promising but require further development of the protocol.

Bibliography

1. Bray, F. *et al.* Global cancer statistics 2018: GLOBOCAN estimates of incidence and mortality worldwide for 36 cancers in 185 countries. *CA: A Cancer Journal for Clinicians* **68**, 394–424 (Nov. 2018).
2. Ulbrich, K. *et al.* Targeted Drug Delivery with Polymers and Magnetic Nanoparticles: Covalent and Noncovalent Approaches, Release Control, and Clinical Studies. eng. *Chemical reviews* **116**, 5338–5431 (May 2016).
3. WHO | Neurological Disorders: Public Health Challenges. *WHO* (2012).
4. Singh, R. & Lillard, J. W. J. Nanoparticle-based targeted drug delivery. eng. *Experimental and molecular pathology* **86**, 215–223 (June 2009).
5. Melgardt M. de VilliersPornanong AramwitGlen S. Kwon. *Nanotechnology in drug delivery* <https://link.springer.com/book/10.1007/978-0-387-77667-5> (2009).
6. Senapati, S., Mahanta, A. K., Kumar, S. & Maiti, P. Controlled drug delivery vehicles for cancer treatment and their performance. *Signal Transduction and Targeted Therapy* **3**, 7 (2018).
7. Sanvicens, N. & Marco, M. P. Multifunctional nanoparticles—properties and prospects for their use in human medicine. eng. *Trends in biotechnology* **26**, 425–433 (Aug. 2008).
8. Veisoh, O., Gunn, J. W. & Zhang, M. Design and fabrication of magnetic nanoparticles for targeted drug delivery and imaging. eng. *Advanced drug delivery reviews* **62**, 284–304 (Mar. 2010).
9. Tan, J., Thomas, A. & Liu, Y. Influence of red blood cells on nanoparticle targeted delivery in microcirculation. *Soft Matter* **8**, 1934–1946 (2012).
10. Owens, D. E. 3. & Peppas, N. A. Opsonization, biodistribution, and pharmacokinetics of polymeric nanoparticles. eng. *International journal of pharmaceutics* **307**, 93–102 (Jan. 2006).
11. Blanco, E., Shen, H. & Ferrari, M. Principles of nanoparticle design for overcoming biological barriers to drug delivery. eng. *Nature biotechnology* **33**, 941–951 (Sept. 2015).
12. Nie, S. Understanding and overcoming major barriers in cancer nanomedicine. *Nanomedicine* **5**, 523–528 (June 2010).
13. Thomsen, L. B. *et al.* Uptake and transport of superparamagnetic iron oxide nanoparticles through human brain capillary endothelial cells. eng. *ACS chemical neuroscience* **4**, 1352–1360 (Oct. 2013).

14. Begley, D. J. Delivery of therapeutic agents to the central nervous system: the problems and the possibilities. *Pharmacology & Therapeutics* **104**, 29–45 (2004).
15. Mikitsh, J. L. & Chacko, A.-M. Pathways for small molecule delivery to the central nervous system across the blood-brain barrier. eng. *Perspectives in medicinal chemistry* **6**, 11–24 (June 2014).
16. Masserini, M. Nanoparticles for brain drug delivery. eng. *ISRN biochemistry* **2013**, 238428 (May 2013).
17. Teleanu, M. D., Negut, I., Grumezescu, V., Grumezescu, M. A. & Teleanu, I. R. *Nanomaterials for Drug Delivery to the Central Nervous System* 2019.
18. Thomsen, L. B., Thomsen, M. S. & Moos, T. Targeted drug delivery to the brain using magnetic nanoparticles. *Therapeutic Delivery* **6**, 1145–1155 (Oct. 2015).
19. Mittal, D. *et al.* Insights into direct nose to brain delivery: current status and future perspective. *Drug Delivery* **21**, 75–86 (Mar. 2014).
20. Pardridge, W. M. CSF, blood-brain barrier, and brain drug delivery. *Expert Opinion on Drug Delivery* **13**, 963–975 (July 2016).
21. Laurent, S. *et al.* Magnetic Iron Oxide Nanoparticles: Synthesis, Stabilization, Vectorization, Physicochemical Characterizations, and Biological Applications. *Chemical Reviews* **108**, 2064–2110 (June 2008).
22. Reddy, L. H., Arias, J. L., Nicolas, J. & Couvreur, P. Magnetic Nanoparticles: Design and Characterization, Toxicity and Biocompatibility, Pharmaceutical and Biomedical Applications. *Chemical Reviews* **112**, 5818–5878 (Nov. 2012).
23. Jain, T. K. *et al.* Magnetic nanoparticles with dual functional properties: drug delivery and magnetic resonance imaging. eng. *Biomaterials* **29**, 4012–4021 (Oct. 2008).
24. Yoo, D., Lee, J.-H., Shin, T.-H. & Cheon, J. Theranostic Magnetic Nanoparticles. *Accounts of Chemical Research* **44**, 863–874 (Oct. 2011).
25. Teja, A. S. & Koh, P.-Y. Synthesis, properties, and applications of magnetic iron oxide nanoparticles. *Progress in Crystal Growth and Characterization of Materials* **55**, 22–45 (2009).
26. Lu, A.-H., Salabas, E. L. & Schüth, F. Magnetic Nanoparticles: Synthesis, Protection, Functionalization, and Application. *Angewandte Chemie International Edition* **46**, 1222–1244 (Feb. 2007).
27. Iwasaki, T., Mizutani, N., Watano, S., Yanagida, T. & Kawai, T. Size control of magnetite nanoparticles by organic solvent-free chemical coprecipitation at room temperature. *Journal of Experimental Nanoscience* **5**, 251–262 (June 2010).
28. Vreeland, E. C. *et al.* Enhanced Nanoparticle Size Control by Extending LaMer’s Mechanism. *Chemistry of Materials* **27**, 6059–6066 (Sept. 2015).

29. Barker, A. J., Cage, B., Russek, S. & Stoldt, C. R. Ripening during magnetite nanoparticle synthesis: Resulting interfacial defects and magnetic properties. *Journal of Applied Physics* **98**, 63528 (Sept. 2005).
30. Park, J. *et al.* Ultra-large-scale syntheses of monodisperse nanocrystals. *Nature Materials* **3**, 891 (Nov. 2004).
31. Hufschmid, R. *et al.* Synthesis of phase-pure and monodisperse iron oxide nanoparticles by thermal decomposition. *Nanoscale* **7**, 11142–11154 (2015).
32. Unni, M. *et al.* Thermal Decomposition Synthesis of Iron Oxide Nanoparticles with Diminished Magnetic Dead Layer by Controlled Addition of Oxygen. *ACS Nano* **11**, 2284–2303 (Feb. 2017).
33. Sun, C., Lee, J. S. H. & Zhang, M. Magnetic nanoparticles in MR imaging and drug delivery. *eng. Advanced drug delivery reviews* **60**, 1252–1265 (Aug. 2008).
34. Narayan, R., Nayak, U. Y., Raichur, A. M. & Garg, S. Mesoporous Silica Nanoparticles: A Comprehensive Review on Synthesis and Recent Advances. *eng. Pharmaceutics* **10** (Aug. 2018).
35. Badruddoza, A. Z. M. *et al.* β -Cyclodextrin conjugated magnetic, fluorescent silica core–shell nanoparticles for biomedical applications. *Carbohydrate Polymers* **95**, 449–457 (2013).
36. Lai, C.-Y. *et al.* A Mesoporous Silica Nanosphere-Based Carrier System with Chemically Removable CdS Nanoparticle Caps for Stimuli-Responsive Controlled Release of Neurotransmitters and Drug Molecules. *Journal of the American Chemical Society* **125**, 4451–4459 (Apr. 2003).
37. Baeza, A., Guisasola, E., Ruiz-Hernández, E. & Vallet-Regí, M. Magnetically Triggered Multidrug Release by Hybrid Mesoporous Silica Nanoparticles. *Chemistry of Materials* **24**, 517–524 (Feb. 2012).
38. Furlani, E. P. in *Electromagnetism* (eds Furlani, E. P. B. T. .-. P. M. & Devices, E.) 1–72 (Academic Press, San Diego, 2001). <http://www.sciencedirect.com/science/article/pii/B9780122699511500024>.
39. Griffiths, D. J. *Introduction to electrodynamics; 4th ed.* Re-published by Cambridge University Press in 2017. <https://cds.cern.ch/record/1492149> (Pearson, Boston, MA, 2013).
40. Moscowitz, B. *Hitchhikers guide to magnetism* 2019. http://www.irm.umn.edu/hg2m/hg2m%7B%5C_%7Da/hg2m%7B%5C_%7Da.html.
41. Pankhurst, Q. A., Connolly, J., Jones, S. K. & Dobson, J. Applications of magnetic nanoparticles in biomedicine. *Journal of Physics D: Applied Physics* **36**, R167–R181 (July 2003).

42. Akbarzadeh, A., Samiei, M. & Davaran, S. Magnetic nanoparticles: preparation, physical properties, and applications in biomedicine. *Nanoscale research letters* **7**, 144 (Feb. 2012).
43. Thanh, N. T. *Magnetic nanoparticles: from fabrication to clinical applications* (CRC press, 2012).
44. Batlle, X. & Labarta, A. *TOPICAL REVIEW: Finite-size effects in fine particles: magnetic and transport properties* (Mar. 2002).
45. P. Guimarães, A. *Principles of Nanomagnetism* (Jan. 2017).
46. Gubin, S. P. *Magnetic Nanoparticles* (2009).
47. Serrano García, R., Stafford, S. & Gun'ko, K. Y. *Recent Progress in Synthesis and Functionalization of Multimodal Fluorescent-Magnetic Nanoparticles for Biological Applications* 2018.
48. Wan, J., Meng, X., Liu, E. & Chen, K. Incorporation of magnetite nanoparticle clusters in fluorescent silica nanoparticles for high-performance brain tumor delineation. *eng. Nanotechnology* **21**, 235104 (June 2010).
49. Wang, F. *et al.* Synthesis of magnetic, fluorescent and mesoporous core-shell-structured nanoparticles for imaging, targeting and photodynamic therapy. *Journal of Materials Chemistry* **21**, 11244–11252 (2011).
50. Chekina, N. *et al.* Fluorescent magnetic nanoparticles for biomedical applications. *Journal of Materials Chemistry* **21**, 7630–7639 (2011).
51. Nacey, A. *Magnetic Drug Targeting: Developing the basics* PhD thesis (2013). <http://hdl.handle.net/1903/14276>.
52. Quanliang, C., Xiaotao, H. & Liang, L. Numerical analysis of magnetic nanoparticle transport in microfluidic systems under the influence of permanent magnets. *Journal of Physics D, Applied Physics* **45**, 12.
53. Nacey, A., Beni, C., Bruno, O. & Shapiro, B. The Behaviors of Ferro-Magnetic Nanoparticles In and Around Blood Vessels under Applied Magnetic Fields. *eng. Journal of magnetism and magnetic materials* **323**, 651–668 (Mar. 2011).
54. Liu, S. & Han, M.-Y. Silica-Coated Metal Nanoparticles. *Chemistry – An Asian Journal* **5**, 36–45 (Jan. 2010).
55. Hermanson, G. T. in (ed Hermanson, G. T. B. T. .-. B. T. (E.) 259–273 (Academic Press, Boston, 2013). <http://www.sciencedirect.com/science/article/pii/B9780123822390000042>.
56. Kotsmar, C. *et al.* Stable Citrate-Coated Iron Oxide Superparamagnetic Nanoclusters at High Salinity. *Industrial & Engineering Chemistry Research* **49**, 12435–12443 (Dec. 2010).

57. Li, Q. *et al.* Correlation between particle size/domain structure and magnetic properties of highly crystalline Fe₃O₄ nanoparticles. *Scientific Reports* **7**, 9894 (2017).
58. Saraswathy, A. *et al.* Citrate coated iron oxide nanoparticles with enhanced relaxivity for in vivo magnetic resonance imaging of liver fibrosis. *Colloids and Surfaces B: Biointerfaces* **117**, 216–224 (2014).
59. Mamani, J. B., Gamarra, L. F. & Brito, G. E. d. S. Synthesis and characterization of Fe₃O₄ nanoparticles with perspectives in biomedical applications. *Materials Research* **17**, 542–549 (2014).
60. Publishing, M. D. *No Title* <http://www.handbookofmineralogy.org/pdfs/maghemite.pdf>.
61. Kemp, S. J., Ferguson, R. M., Khandhar, A. P. & Krishnan, K. M. Monodisperse magnetite nanoparticles with nearly ideal saturation magnetization. *RSC Advances* **6**, 77452–77464 (2016).
62. Sun, S. *et al.* Monodisperse MFe₂O₄ (M = Fe, Co, Mn) Nanoparticles. *Journal of the American Chemical Society* **126**, 273–279 (Jan. 2004).
63. A. Agotegaray & L. Lassalle. *Silica-coated Magnetic Nanoparticles: An Insight into Targeted Drug Delivery and Toxicology* (2017).
64. Xu, W. *et al.* Fluorescein-polyethyleneimine coated gadolinium oxide nanoparticles as T1 magnetic resonance imaging (MRI)–cell labeling (CL) dual agents. *RSC Advances* **2**, 10907–10915 (2012).
65. Kneuer, C. *et al.* Silica nanoparticles modified with aminosilanes as carriers for plasmid DNA. *International journal of pharmaceutics* **196**, 257–261 (Mar. 2000).
66. Magnetite, H. *Magnetite XRD reference peaks* <http://rruff.info/magnetite/R061111> (2019).

Appendix 6

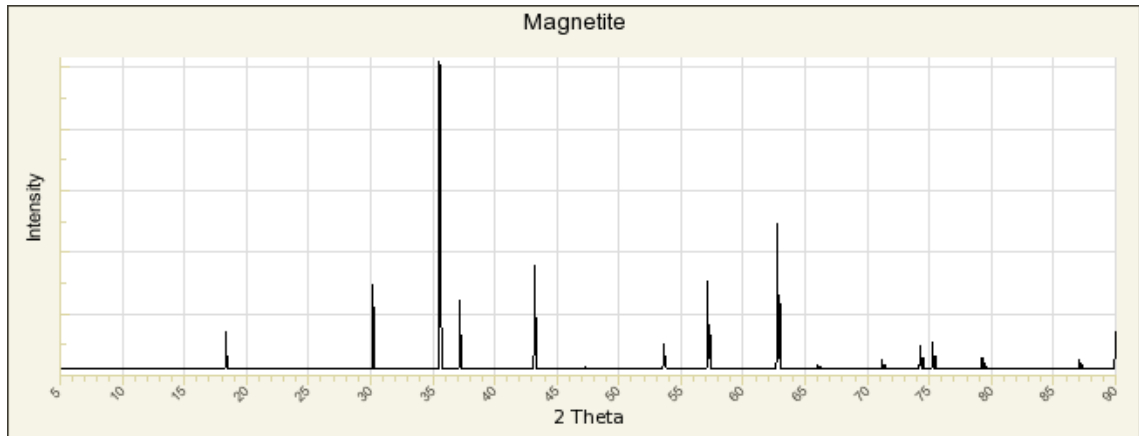


Figure 6.1: XRD reference peaks of magnetite. Adapted from [66]

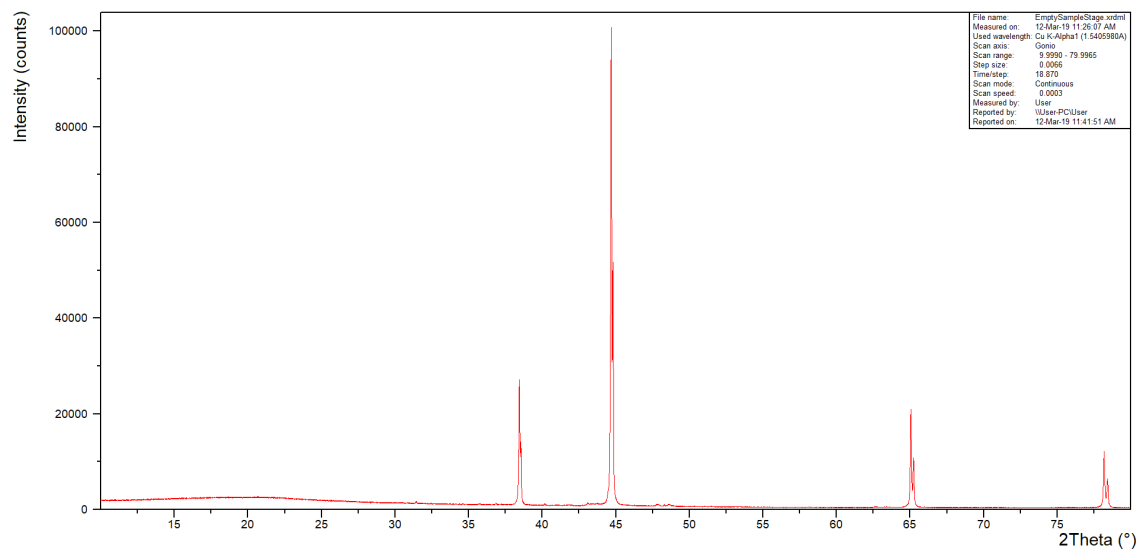


Figure 6.2: XRD spectrum of empty sample stage

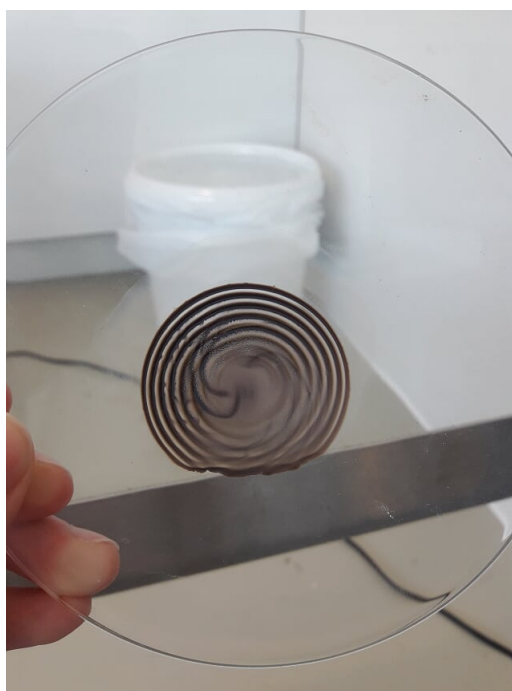


Figure 6.3: IONP drying phenomena